Comparison of basin-scale *in situ* and meteoric ^{10}Be erosion and denudation rates in felsic lithologies across an elevation gradient at the George River, northeast Tasmania, Australia

Leah A. VanLandingham[1], Eric W. Portenga[1], Edward C. Lefroy[2], Amanda H. Schmidt[3], Paul R. Bierman[4], Alan J. Hidy[5]

[1]Geography and Geology Department, Eastern Michigan University, Ypsilanti, MI 48197, United States
[2]Tasmanian Institute of Agriculture, University of Tasmania, Private Bag 98, Hobart 7001, Australia
[3] Geology Department, Oberlin College and Conservatory, Oberlin, OH 44074, United States
[4]Rubenstein School for Natural Resources and the Environment, University of Vermont, Burlington, VT 05405, United States
[5]Center for Accelerator Mass Spectrometry, Lawrence Livermore National Laboratory, Livermore, CA 94550, United States

Correspondence to: Eric W. Portenga (eric.portenga@emich.edu), Paul R. Bierman (paul.bierman@uvm.edu)

Abstract. Long-term erosion rates in Tasmania, at the southern end of Australia's Great Dividing Range, are poorly known; yet, this knowledge is critical for making informed land-use decisions and improving the ecological health of coastal ecosystems. Here, we present quantitative, geologically-relevant estimates of erosion rates for the George River basin, in northeast Tasmania, based on in-situ produced ^{10}Be (^{10}Be$_i$) measured from stream sand at two trunk channel sites and seven tributaries (mean 24.1 ± 1.4 Mg km^{-2} y^{-1}; 1σ). These new ^{10}Be$_i$-based erosion rates are strongly related to elevation, which appears to control mean annual precipitation and temperature, but not slope, suggesting that elevation-dependent surface processes influence rates of erosion in northeast Tasmania. This stands in contrast to erosion rates along the mainland portions of Australia's Great Dividing Range, which are related to basin slope. We also extracted and measured meteoric ^{10}Be (^{10}Be$_m$) from grain coatings of sand-sized stream sediment at each site, which we normalize to measured concentrations of ^{9}Be and use to estimate ^{10}Be$_m$-based denudation rates for the George River. ^{10}Be$_m$-based denudation rates replicate ^{10}Be$_i$ erosion rates within a factor of two, but seem sensitive to recent mining, forestry, and agricultural land use, all of which resulted in widespread topsoil disturbance. Our findings suggest that ^{10}Be$_m$-based denudation metrics can be used to measure landscape dynamics in geologically homogeneous landscapes where recent disturbances to topsoil profiles are minimal.

1 Introduction and the Importance of the George River, Tasmania

Erosion rates of river basins derived from measurements of the in-situ produced cosmogenic isotope, ^{10}Be$_i$, have been used to infer topographic, tectonic, and climatic drivers of landscape evolution for thousands of individual river basins (Codilean et al., 2018; Harel et al., 2016; Mishra et al., 2019; Portenga and Bierman, 2011; Wittmann et al., 2020) and to contextualize the effects of land use on erosion and sediment dynamics (Portenga et al., 2019; Schmidt et al., 2018). Sufficient data now exist that erosion rates from individual studies have been compiled and analysed at the scale of entire continental orogens to demonstrate primary and secondary controls on erosion across thousands to tens of thousands of years (Aguilar et al., 2014; Carretier et al., 2018; Codilean et al., 2021; Delunel et al., 2020; Starke et al., 2020). For example, Delunel et al. (2020) find that $^{10}Be_i$ erosion rates across the European Alps are strongly linked to mean basin slope and influenced by uplift and glaciation. A number of north-south latitudinal studies from the South American Andes show that erosion in some segments of the range is driven by uplift (Carretier et al., 2015; Starke et al., 2017) and slope (Carretier et al., 2018) but not necessarily rainfall unless one considers the effects of vegetation in driving soil weathering rates (Carretier et al., 2015; Starke et al., 2020). A new compilation and analysis of $^{10}Be_i$ erosion rates across the Great Dividing Range of eastern Australia is the first to analyse landscape dynamics across a continent-spanning, passive, post-orogenic rift margin and finds that basin slope is most closely related to erosion at all spatial scales, more so than any other potential driver of erosion (Codilean et al., 2021). While Codilean et al.'s (2021) analysis comprises erosion rates from the western and eastern flanks of the Great Dividing Range—from tropical rainforests in northern Queensland to temperate southeast Victoria—it is restricted to mainland Australia.

Despite the widespread measurement of $^{10}Be_i$ to elucidate erosion rates globally, erosion rate data do not exist for many areas of Earth's surface. Understanding of drivers of erosion will be improved by measuring erosion rates in these understudied areas. In this study, we supplement Codilean et al.'s (2021) erosion compilation with the first $^{10}Be_i$-based erosion rates from the southernmost end of the eastern Australian passive margin on the island-state of Tasmania, specifically the George River basin (Fig. 1). Data in this study are also the first erosion rates measured in temperate rainforests of the Southern Hemisphere (cf. Adams and Ehlers, 2017; Belmont et al., 2007). Quantitative erosion rate data for Tasmania and many of its fluvial systems are currently lacking (Jerie et al., 2003; Koehnken, 2001); data, such as we provide here, are useful information for land managers and for estuary restoration efforts.

The George River empties into Georges Bay (with an 's'), which is known for its oyster stocks (Mitchell et al., 2000) but has been degraded by a history of timber production, tin mining, and agriculture. Historical land-use practices in the catchment have supplied $>10^6$ m^3 of sediment to Georges Bay since the late 19th century (Knighton, 1991) and continue to release pollutants to the Bay (Bleaney et al., 2015; Crawford and White, 2005). The success of efforts to rehabilitate Georges Bay relies in part on reducing sediment delivery from the George River to Georges Bay to pre-disturbance levels (Batley et al., 2010; Crawford and White, 2005; Kragt and Newham, 2009; McKenny and Shepherd, 1999; Mount et al., 2005), but no pre-disturbance erosion data exist for the George River, nor do any geologically-relevant erosion rates exist for any part of Tasmania. Measuring erosion rates for the George River contributes to the growing geomorphological understanding of the drivers of erosion in Tasmania, across Australia, and in similar geological settings elsewhere.

1.1 Quantifying landscape dynamics with *in situ* and meteoric ^{10}Be

The primary goal of this study is to provide background rates (over millennia) of landscape change in the George River basin using the *in situ* cosmogenic isotope beryllium-10 (^{10}Be$_i$) in fluvial sediment (Bierman and Steig, 1996; Brown et al., 1995; Granger et al., 1996). ^{10}Be$_i$ production decreases exponentially with depth in rock and sediment near Earth's surface such that ^{10}Be$_i$ concentrations at depths >2 m are much lower compared to those measured closer to Earth's surface (Gosse and Phillips, 2001; Lal, 1991). ^{10}Be$_i$ produced by muons dominates at depths >2 m (Braucher et al., 2003; Gosse and Phillips, 2001; Heisinger et al., 1997), but muogenic ^{10}Be$_i$ production is negligible when compared to near-surface spallogenic ^{10}Be$_i$ production, except in rapidly eroding landscapes or landscapes with steep terrain (e.g., Dethier et al., 2014; Fellin et al., 2017; Rosenkranz et al., 2018; Scherler et al., 2014; Siame et al., 2011). Bioturbation homogenizes ^{10}Be$_i$ concentrations in soils, in many places to depths of at least ~1 m (Brown et al., 1995; Schaller et al., 2018), and thus ^{10}Be$_i$ erosion rates are largely insensitive to widespread shallow erosion. This insensitivity allows ^{10}Be$_i$ erosion rates to be a useful gauge of pre-disturbance rates of landscape change (Ferrier et al., 2005; Portenga et al., 2019; Schmidt et al., 2018; Vanacker et al., 2007), except where human land use is intensive (i.e., Schmidt et al., 2016) or the effects of human land use are exacerbated by climate extremes (i.e., Rosenkranz et al., 2018). Pre-disturbance ^{10}Be$_i$ erosion data can thus inform approaches to reducing sediment delivery from the George River and support efforts to improve the ecological health of the Georges Bay estuary and possibly other watersheds in northeast Tasmania that share similar bedrock and topographic characteristics by providing a benchmark against which to compare modern sediment loads.

In addition to ^{10}Be$_i$, which is produced in rock and sediment, ^{10}Be is also produced via spallation of oxygen and nitrogen in the atmosphere; this ^{10}Be rains out or falls to Earth's surface (meteoric ^{10}Be; ^{10}Be$_m$; Heikkilä and von Blanckenburg, 2015; Monaghan et al., 1986; Reusser et al., 2010a) where it is readily adsorbed into sediment grain coatings. ^{10}Be$_m$ has traditionally been used to trace sediment through landscapes (Brown et al., 1988; Helz et al., 1992; Portenga et al., 2017; Reusser et al., 2010b; Valette-Silver et al., 1986), but recently derived equations (along with a series of assumptions) now allow denudation rates to be calculated from measurements of ^{10}Be$_m$ that are normalized to non-cosmogenic, stable ^{9}Be, which weathers out of mineral grains (^{9}Be$_{reac}$; von Blanckenburg et al., 2012). ^{10}Be$_m$/^{9}Be$_{reac}$ denudation rates have been used to quantify landscape evolution over a variety of spatial scales for different river basins (^{10}Be$_m$ /^{9}Be$_{reac}$ denudation: Dannhaus et al., 2018; Deng et al., 2020; Portenga et al., 2019; Rahaman et al., 2017; Wittmann et al., 2012, 2015; in some cases ^{10}Be$_m$ is referred to as the reactive phase of ^{10}Be$_m$ [^{10}Be$_{reac}$] and denudation rates may be referred to as ^{10}Be$_{reac}$/^{9}Be$_{reac}$ denudation rates) and have shown promise in quantifying landscape dynamics in quartz-poor landscapes (Deng et al., 2020; Rahaman et al., 2017).

In this study, we use both ^{10}Be$_i$ and ^{10}Be$_m$ /^{9}Be$_{reac}$ to measure the rates at which mass is lost from the George River basin's slopes. Over timescales sufficiently long that the assumption of steady state is approached, all of this mass will transported to the Georges River estuary. Such mass loss form the George basin slopes is both chemical (dissolved load) and physical (sediment transport). The partitioning between these phases differs dramatically around the world depending on rock type, topography, and weathering regime and likely differs within the basin. The assumptions underlying these two methods ($^{10}\mathrm{Be}_{i}$ and $^{10}\mathrm{Be}_{m}$ /$^{9}\mathrm{Be}_{reac}$) differ; results of from each method may not be the same. The concentration of $^{10}\mathrm{Be}_{i}$ is biased towards mass loss within the upper meters of Earth's surface where rates of neutron spallation are high. Both chemical and physical mass losses within this surface layer of regolith are reflected by $^{10}\mathrm{Be}_{i}$ concentrations. $^{10}\mathrm{Be}_{m}$ /$^{9}\mathrm{Be}_{reac}$, if the assumptions of the analytical model are met, reflects both physical and chemical mass loss throughout the regolith, regardless of depth.

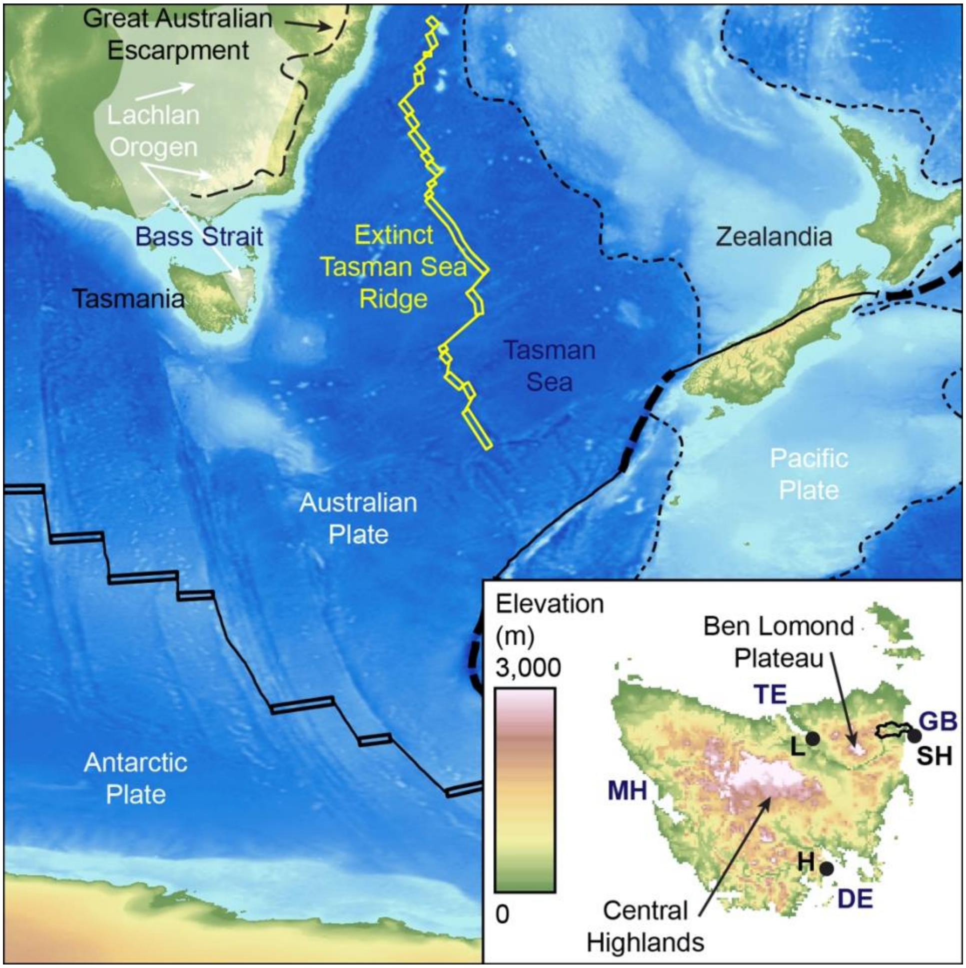

Figure 1: Generalized tectonic map of the eastern Southern Ocean/southwest Pacific Ocean, surrounding Tasmania, including large-scale geologic structures in southeast Australia and Tasmania. Inset shows detailed topography of Tasmania. The main George River basin is shown outlined in black. Major estuaries of other Tasmanian river systems are indicated for reference: Derwent Estuary (DE), Macquarie Harbour (MH), Tamar Estuary (TE), Georges Bay (GB). Cities are shown with black dots for reference: Hobart (H), Launceston (L), St. Helens (SH).

The terms "erosion" and "denudation" have been used without precision in the literature, often as a replacement for one another. Erosion is applied more often to rates calculated using the concentration of $^{10}\mathrm{Be}_{i}$, while rates calculate using $^{10}\mathrm{Be}_{m}$ /$^{9}\mathrm{Be}_{reac}$ are more frequently referred to as denudation. We follow that convention in this paper. Because we have dissolved and suspended load data as well as river flow over time from the mouth of the George River, we attempt to provide a full discussion of what the rates we measure mean for landscape dynamics within the George River Basin.

The small size and relatively uniform bedrock geology of the George River basin provide an ideal location to compare $^{10}\mathrm{Be}_\mathrm{i}$ erosion rates with $^{10}\mathrm{Be}_\mathrm{m}/^{9}\mathrm{Be}_\mathrm{reac}$ denudation rates (von Blanckenburg et al., 2012). $^{10}\mathrm{Be}_\mathrm{m}$ can be desorbed from sediment grain coatings under high pH conditions (Aldahan et al., 1999; You et al., 1989), but $^{10}\mathrm{Be}_\mathrm{m}$ loss from soil profiles in solution is likely minimal in the George River basin because measured soil pH values in the catchment range from 4.0–5.5 (Kidd et al., 2015) and long-term monitoring of stream water pH at two gauging stations—one in Ransom Creek and the other at the George River in St. Helens—shows that stream pH is consistently >5 and mostly >6 (DPIPWE, 2021a,b). The George River basin is a landscape of relative geological homogeneity in comparison to more geologically-diverse landscapes with similar data sets (i.e., Deng et al., 2020; Portenga et al., 2019; Rahaman et al., 2017). Although the George River has a simple bedrock geology, it also has a long history of forestry and lode and placer tin mining that has, in the past, disturbed the hillslopes and fluvial systems (Knighton, 1991; Preston, 2012). Given that land use has affected results of $^{10}\mathrm{Be}_\mathrm{m}$ calculations elsewhere (Portenga et al., 2019), we also explore how land use in the George River affects our interpretations of ^{10}Be-based erosion and denudation calculations in this study.

2 Field Area

Tasmania separated from mainland Australia during Cretaceous rifting of Antarctica and Australia and sits at the southern end of the Great Australian Escarpment—a steep arch-type escarpment that formed during the separation of Zealandia from mainland Australia in the Mid- to Late-Cretaceous (Fig. 1; Codilean et al., 2021; Crowder et al., 2019; Etheridge et al., 1987; Gaina et al., 1998; Griffiths, 1971; Gunn, 1975; Hayes and Ringis, 1973; Lanyon et al., 1993; Matmon et al., 2002; McDougall and van der Lingen, 1974; Mortimer et al., 2017; Persano et al., 2002; Sutherland et al., 2001; Weissel and Hayes, 1977). Bedrock of the George River basin is granodiorite and granite associated with the Blue Tier Batholith, which was emplaced into sediments of the Mathinna Supergroup in the Devonian (Fig. 2; Foster et al., 2000; Gee and Groves, 1971; Gray and Foster, 2004; Higgins et al., 1985; McCarthy and Groves, 1979; Seymour et al., 2006). Siluro-Devonian sedimentary rocks and Neogene basalts underlie small areas, primarily along drainage divides in the central and the western George River basin (Seymour et al., 2006).

The George River basin is of modest size (557 km^2) in northeastern Tasmania with low elevation (mean = 386 m) and gentle hillslopes (mean = 10°). It drains the eastern slopes of the Rattler Range, which currently has a warm, temperate climate (Kottek et al., 2006). Despite eastern Tasmania being in the rain shadow of the central Tasmanian Highlands and western coast ranges, measurements from rainfall gauging stations and temperature data loggers within and near the George River basin show that the local topography of the Ben Lomond Plateau induces strong relationships across the basin between elevation, mean annual precipitation, and mean annual temperature (Fig. 3; Table 1; BoM, 2021; Webb et al., 2018, 2020).

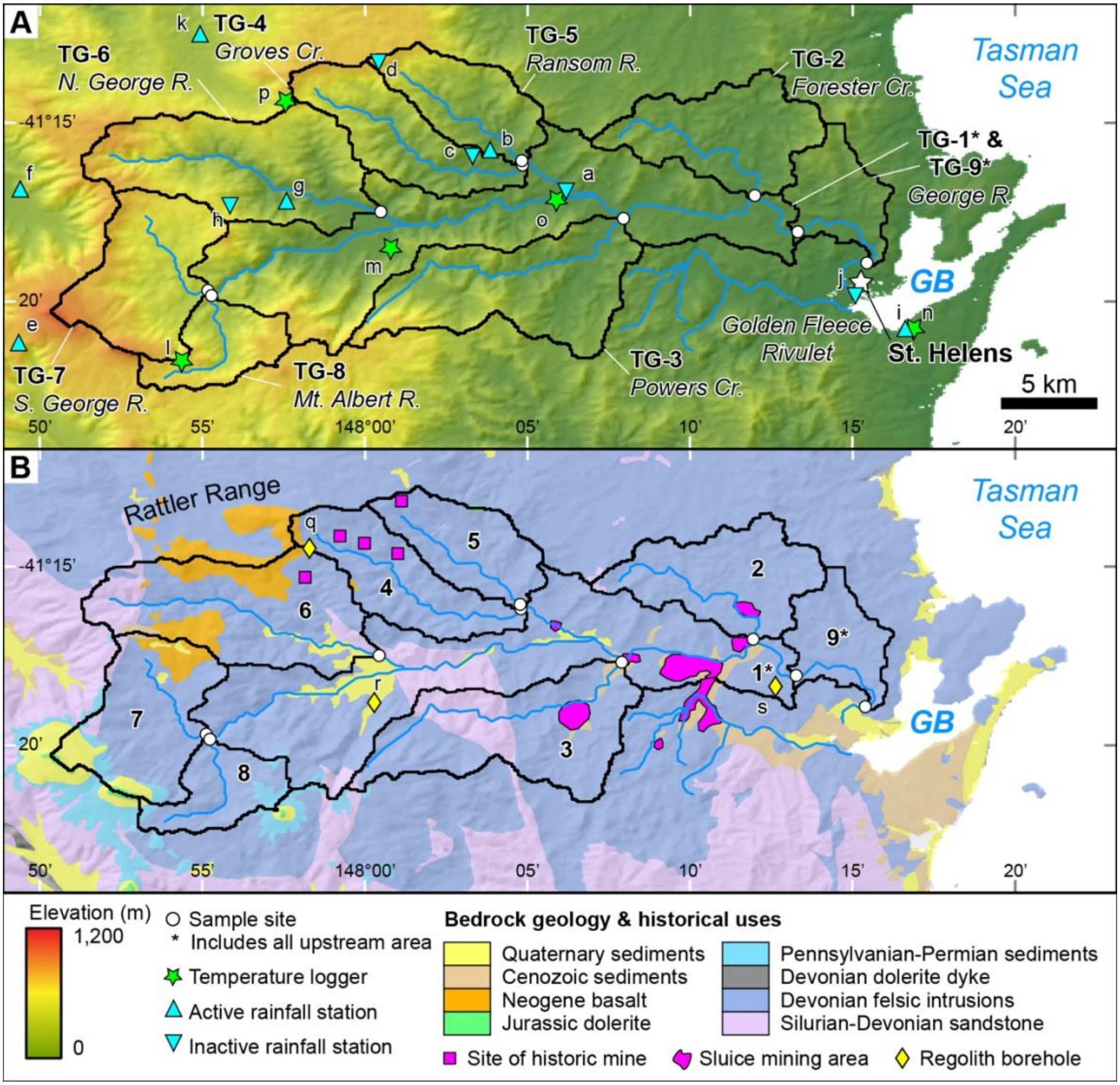

Figure 2: A. Elevation map of the topography of the George River basin. Sample collection sites (white circles), active and inactive Australian Bureau of Meteorology rainfall gauging stations (cyan triangles and cyan inverted triangles, respectively), and temperature logger locations (green stars) are shown (Webb et al., 2018, 2020). B. Bedrock geology map of George River shows the widespread occurrence of Devonian felsic intrusions of the Blue Tier Batholith, which underlies the vast majority of the field area. Note that basins TG-2, TG-4, TG-5, and TG-8 are almost entirely underlain by Devonian felsic intrusions. Areas of historic mining are shown (pink squares and polygons; Knighton, 1991), the action of which delivered >10^6 m^3 to the George River delta in Georges Bay (GB). Locations of boreholes, that strike bedrock are shown by yellow diamonds (BoM, 2015).

Human land use in Tasmania extends to >35 ka, when Aboriginal Australians crossed to the island from the Australian mainland (Cosgrove, 1995; Cosgrove et al., 1990), possibly corresponding to subaerial exposure of the Bass Strait ~56–40 ka (MacIntosh et al., 2006) and localized ice advances in the central Tasmanian highlands (Barrows et al., 2001, 2002; Colhoun, 2002; MacIntosh et al., 2006). Ecological habitat suitability models, based on characteristics and locations of thousands of archaeological sites across Tasmania indicate that Aboriginal communities were located close to freshwater sources and coastal resources, such as the landscapes around Georges Bay and the lower elevations within tributaries to the George River (Jones et al., 2019). Human arrival in Tasmania has been linked to widespread erosion events in mid-elevation landscapes (McIntosh et al., 2009).

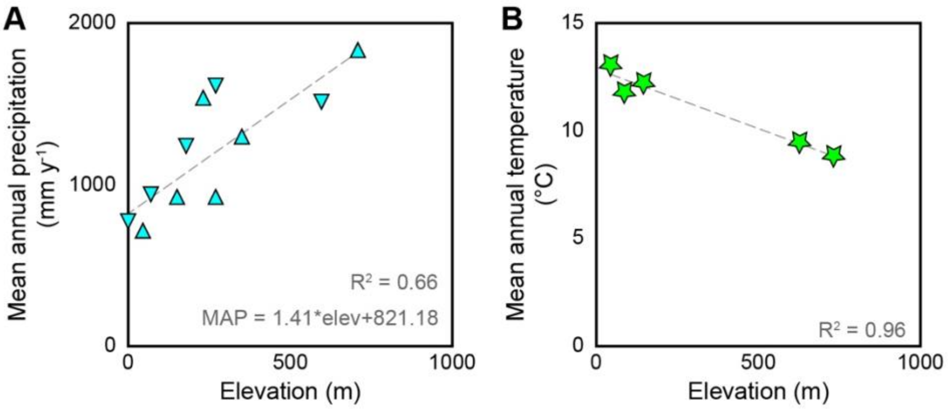

Figure 3: A. Mean annual precipitation from active (cyan triangles) and inactive (inverted cyan triangles) Australian Bureau of Meteorology rainfall gauging stations across George River basin that have at least 1 full year of recorded data exhibiting a strong correlation with station elevation. B. Mean annual temperature (green stars) taken from temperature loggers with >2 years of nearly-daily data showing a strong inverse correlation with elevation. Precipitation and temperature data shown in Table 1.

Table 1. Meteorological and Supplemental Bedrock Data for the George River Basin

Bureau of Meteorology Rainfall Station Name	Figure 2A Map ID	Bur. Of Met. Station ID	Latitude (°)	Longitude (°)	Station Elevation (m)	Data Range[a]	Years of Record	Active?	Mean Annual Precipitation (mm y^{-1})
Goshen (Post Office)	a	92065	-41.27	148.10	76	1965–1970, 1972–1973	8	No	934
Goulds Country	b	92131	-41.24	148.06	237	2005, 2016, 2018, 2020	4	Yes	1503
Goulds Country Post Office	c	92016	-41.25	148.05	183	1885–1895, 1897–1963	78	No	1228
Lottah	d	92022	-41.20	148.00	274	1902–1916, 1918–1935, 1943–1950	41	No	1611
Mt. Victoria (Una Plains)	e	91194	-41.35	147.80	710	1958, 1960, 1962–1964, 1966–1967, 1969, 1971–1974, 2011–2016, 2018–2020	21	Yes	1836
New River (New River Road)	f	91300	-41.27	147.81	274	1997, 2015, 2019–2020	4	Yes	901
Pyengana (Forest Lodge Road)	g	92051	-41.27	147.95	155	1963–1999, 2002, 2005, 2007–2008, 2010–2015, 2017–2020	51	Yes	904
Pyengana (Sea View)	h	92103	-41.28	147.92	598	1988–1992, 1994–2000, 2002, 2005–2006	15	No	1512
St Helens Aerodrome	i	92120	-41.34	148.28	48	2001, 2003–2010, 2012, 2014–2020	16	Yes	681
St Helens Post Office	j	92033	-41.32	148.25	5	1890–1904, 1906–1993, 1995–1999	108	No	777
Weldborough	k	92126	-41.18	147.90	355	2004–2011, 2013–2014, 2016	11	Yes	1265

Temperature Logger Location ID[b]	Figure 2A Map ID	Latitude (°)	Longitude (°)	Logger Elevation (m)	Data Range[b]	Years of Record	Active?	Mean Annual Temperature (°C)
1619552	l	-41.36	147.91	732	2013–2017	5	No	8.8
1620197	m	-41.30	148.01	145	2013–2017	5	No	12.2
1621107	n	-41.34	148.28	44	2013–2017	5	No	13.0
1621175	o	-41.27	148.10	86	2013–2015	3	No	11.8
2623239	p	-41.22	147.96	627	2016–2017	2	No	9.5

Depth to Regolith Borehold ID[c]	Figure 2B Map ID	Latitude (°)	Longitude (°)	Elev. of Top of Bore (m)	Depth to Bedrock through Regolith (m)
17640	q	-41.22409	147.97115	627.8	18.3
40783	r	-41.29352	148.21028	81.1	51.8
41615	s	-41.30384	148.00600	162.0	54.0

[a] Years listed in data ranges are the first and last years for which 12 months of data are available

[b] Temperature logger data sourced from the State of Tasmania Air Temperature Logger Recording Database, used by Webb et al. (2018, 2020). Each year has temperature recorded for at least 30% of days (average = 71%)

[c] Depth to regoltih measured in boreholes (BoM, 2015)

Historically, decades of intensive tin lode mining in isolated headwaters of some tributaries and pockets of hydraulic sluice mining for tin in lowland floodplains introduced >10^6 m^3 of tailings to the George River and its tributaries (Fig. 2a). Knighton (1991) notes that the pre-mining average grain-size of alluvium for the George River was 30–50 mm, and that this was reduced to 1–2 mm during the mining era; however, it is not clear whether the 30–50 mm average grain size was specific to one sample site, or for the George River as a whole. Knighton (1991) notes that bedload characteristics have since returned to their pre-disturbance values following widespread alluvium storage in floodplains and aggradation at the George River delta in Georges Bay (Cheetham and Martin, 2018; Martin and Cheetham, 2018). Despite the George River's return to pre-disturbance channel and bedload characteristics, a study from an experimental forest in the Gentle Annie tributary to the George River shows that sediment yields from logged plots continue to be elevated relative to sediment yields from unlogged plots (Wilson, 1999). More recently, land use within the George River basin in 2008, at the time of sample collection, consisted primarily of forestry production from relatively natural environments and secondarily of conservation land (Fig. 4); intensive land use (i.e., built structures, permanent land alteration) and agricultural production from unirrigated land occur in equal proportion, though much less than the primary and secondary land uses. Only a small percentage of the George River basin is used for agricultural production from irrigated lands (ABARES, 2016).

3 Methods

Sediment samples for this study were collected in 2008 from several locations along the trunk (*n* = 2) and tributaries (*n* = 7) of the George River (Fig. 2; Table 2). At each site, sediment was collected from the streambed and/or in-channel bars to ensure active fluvial transport and mixing. Samples were sieved in the field to the 250–850 μm grain-size fraction. Although this grain-size is finer than the mean natural grain size (30–50 mm; Knighton, 1991), previous studies show that $^{10}Be_i$ grain-size bias is minimal or not present in small, low-elevation, low-relief, temperate landscapes where landslides are uncommon (van Dongen et al., 2019); thus, $^{10}Be_i$ measured from the 250–850 μm grain-size fraction at George River can be interpreted as a geological erosion rate.

$^{10}Be_m$ and the weathered and *in situ* phases of ^{9}Be ($^{9}Be_{reac}$, $^{9}Be_{min}$, respectively) were measured only from the 250–850 μm grain-size fraction from all seven tributary sites (TG-2 through TG-8) and one of the trunk channel sites (TG-9). When $^{10}Be_m$ is normalized to $^{9}Be_{reac}$ following von Blanckenburg et al.'s (2012) denudation rate equation, grain-size biases in resulting $^{10}Be_m/^{9}Be_{reac}$-based denudation rates are diminished (Wittmann et al., 2012). Singleton et al. (2016) also showed the diminishment of grain-size bias for $^{10}Be_m$ measurements when normalized to $^{9}Be_{reac}$. Although it is possible to calculate erosion rates from $^{10}Be_m$ alone (Harrison et al., 2021; Willenbring and von Blanckenburg, 2010), this method does not include any normalization to $^{9}Be_{reac}$, and $^{10}Be_m$ erosion rates are thus susceptible to grain-size bias, especially if the full grain-size distribution is not known and/or has not been analysed. As our samples are of one grain-size fraction and were collected and sieved in the field prior to $^{10}Be_m$ erosion rate derivations, we only present $^{10}Be_m/^{9}Be_{reac}$-based denudation rates in this study.

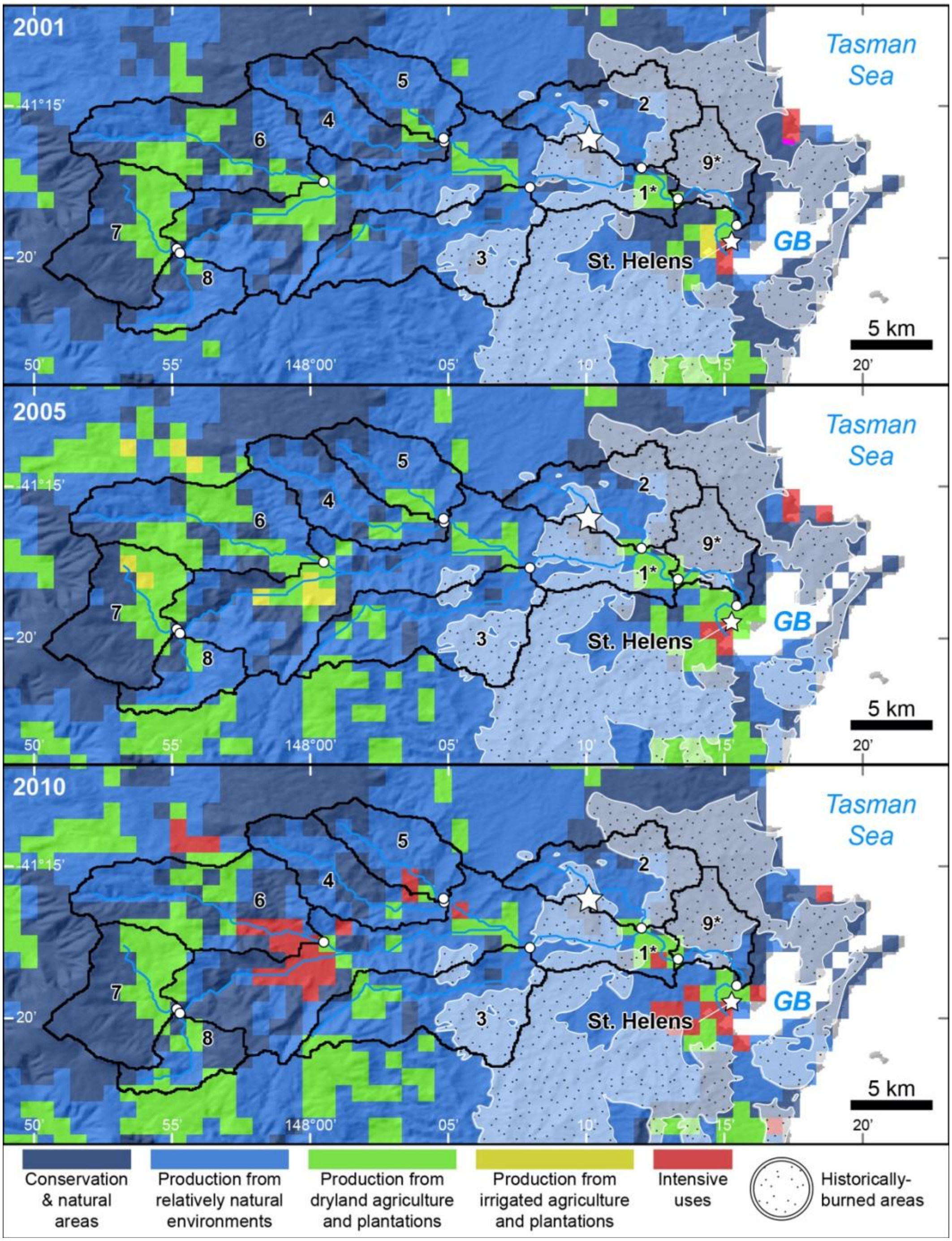

Figure 4: Land cover for each sampled tributary catchment in the George River basin from 2001 (top), 2005 (center), and 2010 (bottom) – the period of leading up to and immediately following sample collection in 2008. The Australian Land Use and Management Classification system groups land use into five primary Classes based on their potential to impact the natural environment (ABARES, 2016). White star denotes location of the Gentle Annie experimental catchment (Wilson, 1999). Stippled areas outlined in white are areas that have been affected by forest fires or prescribed burns in the past (Land Tasmania, 2020). Asterisk (*) indicates trunk channel catchments.

$^{10}Be_i$ was extracted at the University of Vermont from quartz from each sample following standard methods, during which a known amount of a ^{9}Be carrier ($^{9}Be_{carr}$) was added to each sample (Kohl and Nishiizumi, 1992; Corbett et al., 2016); relative to the amount of $^{9}Be_{carr}$, no significant native Be was found in quartz concentrates from any sample, which can otherwise lead to significant overestimates of $^{10}Be_i$-based erosion rates (Portenga et al., 2015). $^{10}Be_i/^{9}Be_{carr}$ ratios were measured by accelerator mass spectrometry at the Lawrence Livermore National Laboratory CAMS facility (Table 3); $^{10}Be_i$ measurements were blank-corrected (the average ratio of three blanks was subtracted from the ratio of each unknown sample) and normalized to the 07KNSTD3110 AMS ^{10}Be standard material, which has a nominal $^{10}Be/^{9}Be$ ratio of 2.85×10^{-12} (Nishiizumi et al., 2007). $^{10}Be_i$ production was averaged across all sampled basins to a single point following Portenga and Bierman (2011), and the online erosion rate calculator described by Balco et al. (2008), which has been subsequently updated, was used to derive $^{10}Be_i$ erosion rates following the Lal (1991) and Stone (2000) scaling schemes (ε, Tables 4, 5). Here, ε is presented in units of Mg km^{-2} ky^{-1} (Table 5) allowing us to compare measures of ε directly with $^{10}Be_m/^{9}Be_{reac}$-based denudation rates (D_m; see below). Muogenic production of $^{10}Be_i$ is incorporated into ε; however, muogenic $^{10}Be_i$ is negligible relative to spallogenic $^{10}Be_i$ production given the George River's post-orogenic, low-elevation, low-relief setting.

$^{10}Be_m$ was extracted following Stone's (1998) fusion method and a ^{9}Be carrier solution was added to each sample. Through this process, some amount of $^{10}Be_i$ from bulk sediment is incorporated into the $^{10}Be_m$ sample; however, the amount of $^{10}Be_i$ is negligible, consistently two orders of magnitude less than $^{10}Be_m$ measurements (Table 3). $^{10}Be_m/^{9}Be_{carr}$ ratios of these fusion extracts were measured at the Lawrence Livermore National Laboratory CAMS facility, blank-corrected (ratio of one blank was subtracted from ratio of each unknown sample; Table 3) and normalized to the 07KNSTD3110 standard material (Nishiizumi et al., 2007). Sample material used to calculate $^{9}Be_{reac}$ was first subject to 6N HCl acid leaching to remove sediment grain coatings (Greene, 2016; Portenga et al., 2019 supplement); it was then fully digested in HF and $^{9}Be_{min}$ was measured in that solution. Both $^{9}Be_{reac}$ from sediment grain coatings and $^{9}Be_{min}$ from the remaining mineral material were measured by inductively coupled plasma-optical emission spectrometry (ICP-OES) at the University of Vermont. Together, these data were used to derive denudation rates following von Blanckenburg et al. (2012; Table 4). At the time of sample collection (2008), the equations to calculate D_m had not been published, and bedrock samples from the field area were not collected. We therefore rely on using a global crustal average of 2.5 ppm for the amount of native ^{9}Be in our samples (von Blanckenburg et al., 2012). In this study, D_m is presented in units of Mg km^{-2} y^{-1} (Table 5).

Values for the rate at which $^{10}Be_m$ is delivered from the atmosphere to Earth's surface ($^{10Be}F_{met}$) have been measured and modelled in various ways at both local and global scales, each with its own strengths. For instance, in the southwest Pacific region, Reusser et al. (2010a) directly measured $^{10Be}F_{met}$ in a dated New Zealand paleosol (1.68 to 1.72×10^{6} atoms cm^{-2} y^{-1}). In the absence of direct measurement, $^{10Be}F_{met}$ must be estimated or modelled. Heikkilä and von Blanckenburg integrate $^{10Be}F_{met}$ through the Holocene while others integrate $^{10Be}F_{met}$ for total atmospheric thickness, all at a global scale (Masarik and Beer, 2009; Willenbring and von Blanckenburg, 2010), but the resolution of these models is not fine-enough for the small spatial scale of this study, and $^{10Be}F_{met}$ would be the same for each sampled basin (1.0–1.5 x 10^6 atoms cm^{-2} y^{-1} for Holocene integrated or ~7 x 10^5 atoms cm^{-2} y^{-1} for atmospheric depth-integrated $^{10Be}F_{met}$). Graly et al. (2011), however, present an equation that estimates $^{10Be}F_{met}$ from a location's mean annual precipitation and latitude, which provides a more specific value for $^{10Be}F_{met}$ for any selected study site. Here, we use estimated values of $^{10Be}F_{met}$ based on Graly et al.'s (2011) model because it provides an estimate of $^{10Be}F_{met}$ that is specific for each sampled basin in this study; these values range from 8.55 x 10^5 atoms cm^{-2} y^{-1} to 1.46 x 10^6 atoms cm^{-2} y^{-1}, which are of the same order of magnitude as $^{10Be}F_{met}$ measured in New Zealand (Reusser et al., 2010a) or those based on global $^{10Be}F_{met}$ models (Heikkilä and von Blanckenburg, 2015; Masarik and Beer, 2009; Willenbring and von Blanckenburg, 2010). We use mean annual precipitation values calculated from our own correlation of gauging stations against elevation (Figure 3A) because of inconsistencies, described below, between measured data and modelled data in our study area.

Table 2. Sample locations and topographical basin data

Sample ID	Sample Location			Basin-average elevation (m)^a	Basin Area (km^2)^a	Mean local relief (m)^a	Mean Basin slope (°)^a	Mean Annual Precipitation (mm y^{-1})^b	% of Tributary with >"High" Erosivity^c
	River name	Latitude (°)	Longitude (°)						
TG-1	George River	-41.29017	148.22217	346	397.25	218.0	10	1,310	
TG-2	Forester Creek	-41.27183	148.19925	141	40.21	120.0	6	1,020	9.2
TG-3	Powers Creek	-41.28286	148.13247	265	55.56	214.8	10	1,195	38
TG-4	Groves Creek	-41.25514	148.08317	364	34.39	238.0	11	1.336	49.5
TG-5	Ransom River	-41.25364	148.08239	347	27.71	226.8	10	1.312	48.8
TG-6	North George River	-41.28067	148.00697	439	65.84	275.5	12	1,442	49.3
TG-7	South George River	-41.32208	147.92172	652	42.53	211.5	9	1,743	26.9
TG-8	Mt. Albert Rivulet	-41.32178	147.92592	596	20.42	227.8	10	1,663	40.4
TG-9	George River @ St. Helens	-41.31350	148.26531	331	426.88	213.5	10	1,289	

[a] Based or derived from Satellite Radar Topography Mission data, 90 m resolution (Gallant et al., 2011). Mean local relief calculated using a 10-cell (~900 m) circular moving window.

[b] Used in the calculation of the meteoric ^{10}Be delivery rate, $^{10Be}F_{met}$, for each catchment (Graly et al., 2011). Calculated using the basin average elevation and using the regression equation betwee and mean annual precipitation at Australian Bureau of Meteorology stations (Figures 2, 3; Table 1).

[c] Erosivity ratings from Kidd et al. (2014, 2015).

Table 3. Isotope data

In situ Sample ID	UVM Batch No.	Quartz mass (g)	Carrier mass (μg)	LLNL Sample ID	$^{10}Be_i/^9Be_{carr}$	± 1σ	$^{10}Be_i$ (atoms g^{-1})	± 1σ
TG-1	432^a	20.099	250.791	BE28820	4.37E-13	7.83E-15	3.64E+05	6.52E+03
TG-2	438^b	20.100	249.506	BE29129	6.83E-13	9.31E-15	5.66E+05	7.72E+03
TG-3	438	22.423	249.704	BE29130	4.79E-13	1.41E-14	3.97E+05	1.17E+04
TG-4	438	19.288	248.814	BE29131	3.10E-13	8.41E-15	2.56E+05	6.95E+03
TG-5	438	20.702	250.296	BE29133	4.37E-13	1.02E-14	3.63E+05	8.48E+03
TG-6	446^c	20.532	249.209	BE29303	2.81E-13	6.11E-15	2.33E+05	5.05E+03
TG-7	446	20.156	249.111	BE29304	2.28E-13	6.76E-15	1.88E+05	5.60E+03
TG-8	446	20.747	249.704	BE29305	2.99E-13	7.35E-15	2.48E+05	6.10E+03
TG-9	446	20.169	250.791	BE29306	4.94E-13	1.19E-14	4.11E+05	9.92E+03

Meteoric Sample ID	UVM Batch No.	Sample mass (g)	Carrier mass (μg)	LLNL Sample ID	$^{10}Be_m/^9Be_{carr}$	± 1σ	$^{10Be}F_{met}$ (atoms cm^{-2} y^{-1})	$^{10}Be_m$ (atoms g^{-1})	± 1σ	$^9Be_{min}$ (atoms g^{-1})	$^9Be_{reac}$ (atoms g^{-1})
TG-2	MB-15^d	0.463	328.71	BE27783	1.51E-12	2.07E-14	8.12E+05	7.16E+07	9.83E+05	2.51E+16	1.32E+16
TG-3	MB-15	0.497	298.02	BE27784	1.50E-12	2.26E-14	8.92E+05	5.99E+07	9.05E+05	3.19E+16	1.06E+16
TG-4	MB-15	0.457	296.04	BE27785	1.12E-12	1.55E-14	9.73E+05	4.84E+07	6.69E+05	3.29E+16	1.08E+16
TG-5	MB-15	0.491	300.00	BE27786	1.05E-12	1.46E-14	9.79E+05	4.29E+07	5.95E+05	2.84E+16	1.09E+16
TG-6	MB-15	0.466	300.99	BE27787	4.30E-12	5.79E-14	1.01E+06	1.85E+08	2.50E+06	4.54E+16	4.06E+16
TG-7	MB-15	0.487	299.01	BE27788	5.60E-12	6.09E-14	1.06E+06	2.30E+08	2.50E+06	3.09E+16	5.82E+16
TG-8	MB-15	0.487	300.00	BE27789	5.35E-12	5.83E-14	1.01E+06	2.20E+08	2.40E+06	2.71E+16	5.54E+16
TG-9	MB-15	0.541	299.01	BE27790	1.19E-12	1.64E-14	9.28E+05	4.39E+07	6.06E+05	1.53E+16	1.08E+16

[a] In situ Batch 432 Blank $^{10}Be_i/^9Be_{carr}$ ratio = 1.25 x 10^{-14} ± 5.87 x 10^{-16}

[b] In situ Batch 438 Blank $^{10}Be_i/^9Be_{carr}$ ratio = 1.22 x 10^{-14} ± 1.82 x 10^{-15}

[c] In situ Batch 446 Blank $^{10}Be_i/^9Be_{carr}$ ratio = 1.27 x 10^{-14} ± 6.70 x 10^{-16}

[d] Meteoric Batch MB-15 Blank $^{10}Be_m/^9Be_{carr}$ ratio = 1.65 x 10^{-14} ± 1.72 x 10^{-15}

We compare ε and D_m to various topographic and land-use factors to assess possible processes driving or related to background landscape evolution in the George River (Tables 1, 2). Topographic data are derived from the SRTM 90-m resolution global dataset (Gallant et al., 2011). Mean local relief was calculated over a moving 10-cell (~900 m) circular window. We do not compare ε or D_m to climate data from global gridded datasets for mean annual temperature and mean annual precipitation, although such data are available. This is because the gridded datasets are all models based on limited measurements and include a strong elevation component in their interpolation scheme (e.g. WorldClim, Fick and Hijmans, 2017) or have spatial resolutions that do not provide sufficient detail for the small size of the George River basin (e.g. TRMM, Huffman, 2021). These characteristics of gridded climate datasets makes it difficult to attribute erosion to climatic drivers independent of their self-correlation with elevation. Thus, we rely on observed relationships between elevation and precipitation and temperature data from precipitation gauges (n = 10, each with >4 years of daily data; Table 1, Figs. 2, 3) and temperature loggers (n = 5, each with >2 years of hourly data from at least 30% of days reporting [average = 70% of days reporting]; Table 1, Figs. 2, 3). Although the spatial coverage of rainfall gauges and temperature loggers is small relative to the coverage of interpolated, modelled, gridded data, they provide us an opportunity to work with real measured data

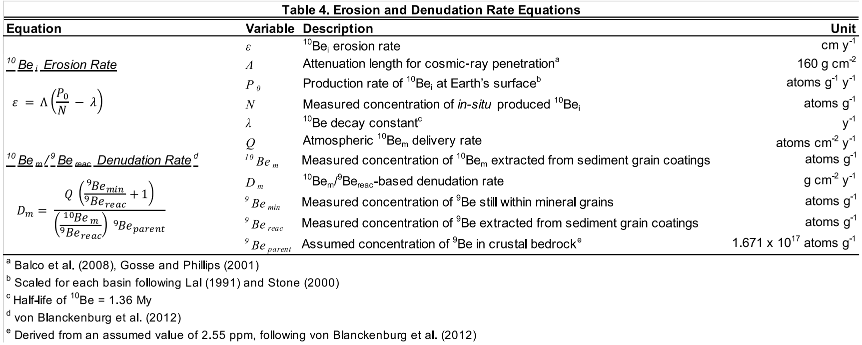

Table 4. Erosion and Denudation Rate Equations

Equation	Variable	Description	Unit
	ε	$^{10}Be_i$ erosion rate	cm y^{-1}
$^{10}Be_i$ Erosion Rate	Λ	Attenuation length for cosmic-ray penetration[a]	160 g cm^{-2}
	P_0	Production rate of $^{10}Be_i$ at Earth's surface[b]	atoms g^{-1} y^{-1}
$\varepsilon = \Lambda\left(\frac{P_0}{N} - \lambda\right)$	N	Measured concentration of *in-situ* produced $^{10}Be_i$	atoms g^{-1}
	λ	^{10}Be decay constant[c]	y^{-1}
	Q	Atmospheric $^{10}Be_m$ delivery rate	atoms cm^{-2} y^{-1}
$^{10}Be_m/^{9}Be_{reac}$ Denudation Rate[d]	$^{10}Be_m$	Measured concentration of $^{10}Be_m$ extracted from sediment grain coatings	atoms g^{-1}
	D_m	$^{10}Be_m/^{9}Be_{reac}$-based denudation rate	g cm^{-2} y^{-1}
$D_m = \frac{Q\left(\frac{^{9}Be_{min}}{^{9}Be_{reac}}+1\right)}{\left(\frac{^{10}Be_m}{^{9}Be_{reac}}\right)\,^{9}Be_{parent}}$	$^{9}Be_{min}$	Measured concentration of ^{9}Be still within mineral grains	atoms g^{-1}
	$^{9}Be_{reac}$	Measured concentration of ^{9}Be extracted from sediment grain coatings	atoms g^{-1}
	$^{9}Be_{parent}$	Assumed concentration of ^{9}Be in crustal bedrock[e]	1.671 x 10^{17} atoms g^{-1}

[a] Balco et al. (2008), Gosse and Phillips (2001)

[b] Scaled for each basin following Lal (1991) and Stone (2000)

[c] Half-life of ^{10}Be = 1.36 My

[d] von Blanckenburg et al. (2012)

[e] Derived from an assumed value of 2.55 ppm, following von Blanckenburg et al. (2012)

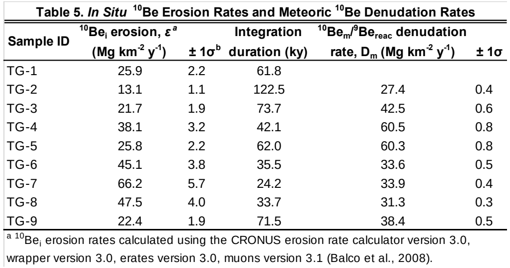

Table 5. *In Situ* ^{10}Be Erosion Rates and Meteoric ^{10}Be Denudation Rates

Sample ID	$^{10}Be_i$ erosion, ε[a] (Mg km^{-2} y^{-1})	± 1σ[b]	Integration duration (ky)	$^{10}Be_m/^{9}Be_{reac}$ denudation rate, D_m (Mg km^{-2} y^{-1})	± 1σ
TG-1	25.9	2.2	61.8		
TG-2	13.1	1.1	122.5	27.4	0.4
TG-3	21.7	1.9	73.7	42.5	0.6
TG-4	38.1	3.2	42.1	60.5	0.8
TG-5	25.8	2.2	62.0	60.3	0.8
TG-6	45.1	3.8	35.5	33.6	0.5
TG-7	66.2	5.7	24.2	33.9	0.4
TG-8	47.5	4.0	33.7	31.3	0.3
TG-9	22.4	1.9	71.5	38.4	0.5

[a] $^{10}Be_i$ erosion rates calculated using the CRONUS erosion rate calculator version 3.0, wrapper version 3.0, erates version 3.0, muons version 3.1 (Balco et al., 2008).

Proper interpretation of $^{10}Be_m$ derived denudation rates requires an understanding of the potential for beryllium weathering and desorption from sediment grain coatings and mobility through regolith (von Blanckenburg et al., 2012). To this end, information on (1) the depth of regolith and (2) chemical weathering data across the George River basin are needed. A potentially relevant dataset available for Tasmania is an interpolated gridded map of depth of regolith (Wilford et al., 2016). However, like the WorldClim precipitation and temperature datasets, the gridded regolith dataset was created by interpolating measured data from around Australia using a model and has an implicit dependence on elevation that does not reflect measured depths to bedrock in the George River basin. Only three boreholes exist in the George River basin that clearly go through regolith to bedrock, from which we extracted regolith depth (BoM, 2015; Fig. 2A; Table 1). They do not match the model results. These three boreholes, and others in the study area, have some units that could be alluvium or regolith; this differentiation is not clear and therefore the depth of regolith could be overestimated if alluvium is marked as regolith. Thus, we cannot know with certainty the depth of regolith across our field area and we therefore cannot draw any clear conclusions about beryllium mobility in deep, weathered soils from the borehole data alone and do not explore it further.

There is one long term water quality and stream gauging station in the George River basin. It is at the inlet to the local water treatment plant for the trunk channel of the George River in the town of St. Helens (Fig. 2). Thus, we can only estimate the degree of chemical weathering for the entire George River basin, not individual tributaries. Chemical weathering rates for the George River at St. Helens were calculated using water quality data (i.e., dissolved major and trace element data) and discharge data (J. Fawcett, TasWater, pers. comm. 2021). Discharge measurements were taken at intervals ranging from 4 to 96 times per day from 1968 to 2021; 26 complete years of discharge data were available. Water quality measurements have been conducted since 2015 and we used the data from July 2015 to September 2021 in our derivation of chemical weathering for the George River basin. We matched water quality measurements with the nearest discharge measurement in time; when times did not line up exactly, we used the average of the nearest two discharge measurements (Table 6). We then explored the relationship between discharge and each water quality parameter. For parameters that are invariant with discharge (iron, potassium, sulphate, silica), we calculated the mean concentration of the parameter. For parameters that scale with discharge (calcium, magnesium), we used a rating curve to determine how discharge relates to each water quality parameter; we then applied the mean measured values and rating curves, as appropriate, to every discharge measurement for years with complete discharge records. Sodium and chlorine were balanced (suggesting a sea salt contribution) and were thus omitted from the calculation. Carbonate that balanced the calcium and magnesium present was included; the rest was assumed to be from atmospheric sources. Silica concentrations were measured independently, once annually from 1974 to 1981 (J. Fawcett, TasWater, pers. comm. 2021), and we used all eight of those measurements; measurements in individual years were taken in March, June, August, October, and November. We report total dissolved solids (TDS) measurements that are the sum of potassium, sulphate, silica, calcium, magnesium, and carbonate concentrations following West et al. (2005)’s chemical weathering rate calculation. We used a similar method to calculate the total suspended sediment (TSS) for each year of complete discharge data; TSS scales with discharge and so we applied a rating curve.

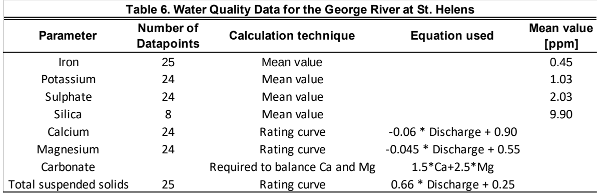

Table 6. Water Quality Data for the George River at St. Helens

Parameter	Number of Datapoints	Calculation technique	Equation used	Mean value [ppm]
Iron	25	Mean value		0.45
Potassium	24	Mean value		1.03
Sulphate	24	Mean value		2.03
Silica	8	Mean value		9.90
Calcium	24	Rating curve	-0.06 * Discharge + 0.90	
Magnesium	24	Rating curve	-0.045 * Discharge + 0.55	
Carbonate		Required to balance Ca and Mg	1.5*Ca+2.5*Mg	
Total suspended solids	25	Rating curve	0.66 * Discharge + 0.25	

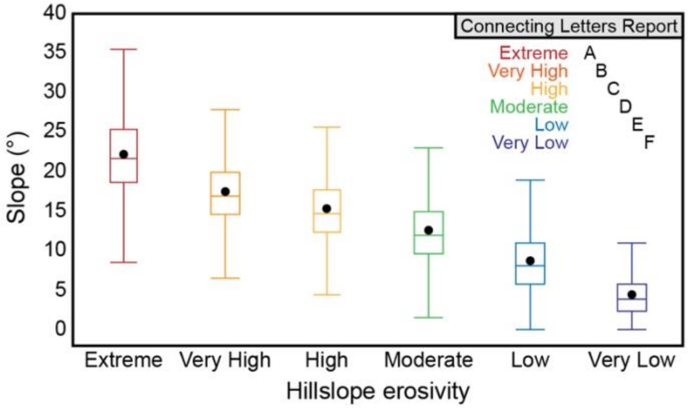

Figure 5: Analysis of variance, showing hillslope angles associated with categories of landscape erosivity (Kidd et al., 2014, 2015) at George River. Box-and-whiskers cover ±1.5x the interquartile range; black dot is the mean slope for the erosivity category. The mean slope for each erosivity category is significantly different from every other category, illustrated by the Connecting Letters Report (if the mean slope in any two erosivity categories were statistically indistinguishable, they would otherwise share a letter in the report). We therefore use hillslope angle as a quantitative proxy for erosivity in the George River basin.

Lastly, qualitative ratings of soil erosivity have previously been determined for Tasmania (Kidd et al., 2014, 2015) based on modelled soil loss should substantial vegetation and ground cover be removed; these ratings are strongly tied to hillslope angle within the George River basin (Fig. 5). Additionally, slope and erosion are strongly linked across the Great Dividing Range on the Australian mainland (Codilean et al., 2021). Thus, we compare erosion and denudation metrics against basin slope metrics, which enables us to compare our measures of ε and D_m to basin slope to assess how Kidd et al.'s (2014, 2015) metrics for of hillslope erodibility and erosion in the George River are related and to compare these new $^{10}Be_i$ erosion rates to those presented by Codilean et al. (2021) for the Australian mainland.

4 Results

4.1 ^{10}Be$_i$ erosion rates, ε

Erosion rates, ε, based on measured concentrations of $^{10}Be_i$ range from 13.1 to 66.2 Mg km^{-2} y^{-1}. They integrate landscape dynamics in the George River basin since ~24–122 ka (Table 4). The average ε from tributaries (36.8 ± 1.3 Mg km^{-2} y^{-1}) is greater than from either of the trunk channel samples (TG-1 = 25.9 ± 2.2 Mg km^{-2} y^{-1}; TG-9 = 22.4 ± 1.9 Mg km^{-2} y^{-1}). Tributary values for ε are greater in the high-elevation, western headwaters of the George River basin and decrease systematically, eastwards towards the lower-elevation coast (Fig. 6; $R^2 = 0.91$, $p < 0.001$). Relationships between ε in tributary catchments and mean local relief, mean basin slope, and the percent of each basin that is categorized as being greater than or equal to "High" Erosivity are weak and not significant ($R^2 = 0.28$, $R^2 = 0.17$, $R^2 = 0.05$, respectively, $p \geq 0.13$). Taking the product of ε and basin area provides us with the average annual mass loss for each catchment. Making the assumption of steady state and no change in storage over time, we can then compare mass export rates across the catchment. Following this approach, we find that a similar mass exited sampled tributaries (10,511 ± 394 Mg y^{-1}) as the mass that passes through the trunk channel sites (TG-1 = 10,286 ± 859 Mg y^{-1}; TG-9 = 9,555 ± 817 Mg y^{-1}). This comparison suggests little to no contribution of mass from the lowland, mainstem George River valley below the tributaries and above the basin outlet sampling sites.

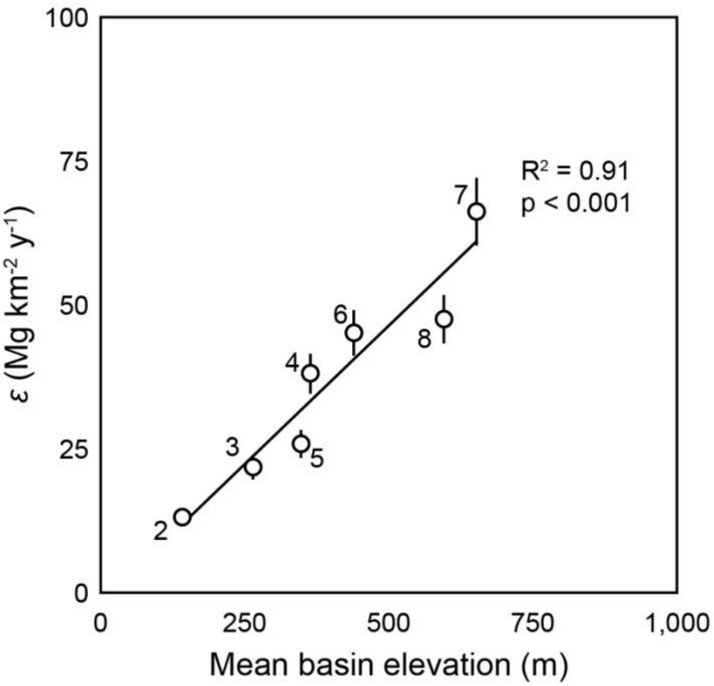

Figure 6: A strong correlation between $^{10}Be_i$ based erosion rates (ε) and mean basin elevation for the seven tributary samples collected in this study. We do not include data from trunk channel samples because they may incorporate sediment upstream of trunk channel sites but downstream of tributary sites (see Discussion).

4.2 $^{10}Be_m$ denudation rates, D_m

$^{10}Be_m/^9Be_{reac}$-based denudation rates, D_m, range from 27.4 to 60.5 Mg km^{-2} y^{-1}. Values for D_m in tributaries do not replicate $^{10}Be_i$-derived erosion rates, ε, in any basin (Fig. 7). Neither does the $^{10}Be_m/^9Be_{reac}$-based denudation rate at the trunk channel site, TG-9 (38.4 ± 0.5 Mg km^{-2} y^{-1}), replicate the $^{10}Be_i$ erosion rate (22.4 ± 1.9 Mg km^{-2} y^{-1}). In general, $^{10}Be_m$-based measures D_m of tributaries are not significantly related to any topographic or basin metric such as mean basin elevation, mean local relief, or mean basin slope ($R^2 = 0.12$, $R^2 = 0.06$, $R^2 = 0.11$, respectively; $p > 0.44$). $^{10}Be_m$-based measures D_m of tributaries appear to be moderately related to the percentage of each basin that Kidd et al. (2014, 2015) categorizes with a land use of “High” to “Extreme” erosivity, though we note this relationship is not significant ($R^2 = 0.42$; $p = 0.18$; Fig. 8).

4.3 Dissolved load and suspended sediment fluxes

The total dissolved sediment load in the George River at St. Helens for the 26 years between 1969 and 2020 is between 1,820 and 10,770 Mg y^{-1} (mean = 4,400 ± 2,230 Mg y^{-1}, 1σ) and the total suspended sediment load ranges from 280 to 10,560 Mg y^{-1} (mean = 1,830 ± 2,180 Mg y^{-1}, 1σ). The water treatment plant from which the dissolved load data were obtained is close to site TG-9, and data from this site allow us to place ^{10}Be-inferred erosion and denudation rates for the whole George River basin in context. These data show that the dissolved load export rate averages to about 10.3 Mg km^{-1} y^{-1}, which is <50% of ε (22.4 Mg km^{-2} y^{-1}), based on decades of flow records and five years of discontinuous water sampling at the same sampling location. The suspended sediment export rate out of the George River basin is less, 4.3 Mg km^{-2} y^{-1}.

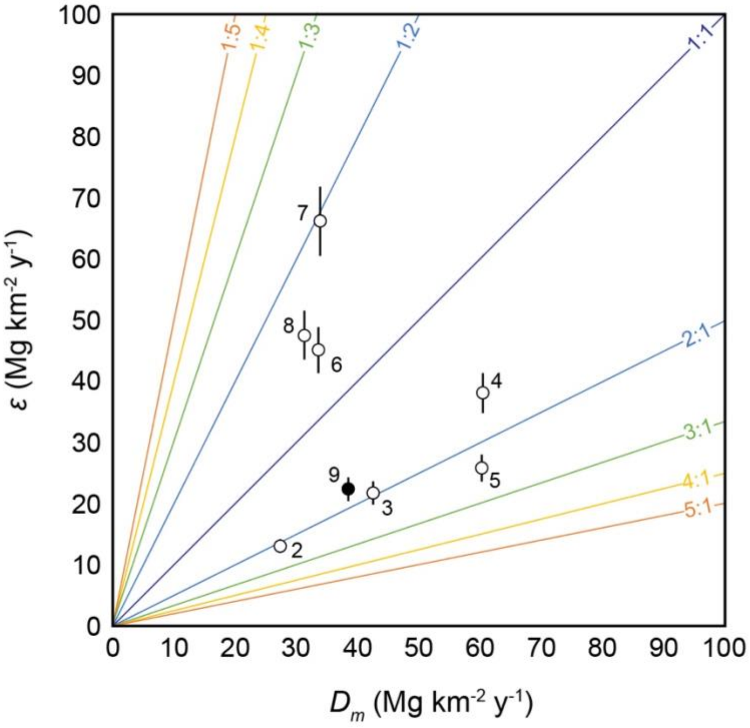

Figure 7: ^{10}Be$_i$ based erosion rates (ε) compared ^{10}Be$_m$/^{9}Be$_{reac}$-based denudation rates (D_m) for tributary basins (open circles) and the trunk channel site, TG-9 (closed circle). Measures of ε and D_m are different at each site, but similar within a factor of two.

5 Discussion

The multi-methodological approach we employ in this study provides four new datasets, all of which quantify some component of landscape change at different spatial scales: (1) mass loss rates inferred ^{10}Be$_i$ at seven tributary and two trunk channel sites, (2) denudation rates from ^{10}Be$_m$/^{9}Be$_{reac}$ from seven tributary sites and one trunk channel site, (3) suspended sediment export at the mouth of the George River, and (4) the dissolved load of the George River from the water quality and flow data at the mouth of the catchment. Comparing and interpreting these new datasets improves our understanding of the rate of landscape change over time in the George River basin. Given that the only location for which we have data from all four of datasets is at the mouth of the George River in St. Helens, we explore what the different rates presented in this study might mean for landscape change across the whole river basin, recognizing that without more data, we cannot be more specific in our interpretation of ε or D_m at tributary sites beyond traditional meanings of erosion or denudation, respectively.

5.1 Relationships between ε, elevation-dependent climate conditions, and land use

Erosion rates in the George River basin are strongly related to basin elevation, which varies greatly across the catchment as the study area extends east from the Rattler Range and Mt. Victoria (1,213 m) to the coast at sea-level (Fig. 2). In contrast, we find no evidence to suggest that ε is related to slope in the George River over millennial timescales. This result differs from many studies, which show strong correlations between ε and mean basin slope at a global scale (Portenga and Bierman, 2011) and at regional scales across the Great Dividing Range on Australia's mainland (Fig. 9; Codilean et al., 2021; Nichols et al., 2014). Our results also differ from prior assessments of the George River basin using measured climate data, bedrock structure, topographic analysis, water quality models, and geographical landscape characterization that suggest slope imparts a large control over erosion and sediment generation in the catchment on human timescales (Jerie et al., 2003; Kragt and Newham, 2009).

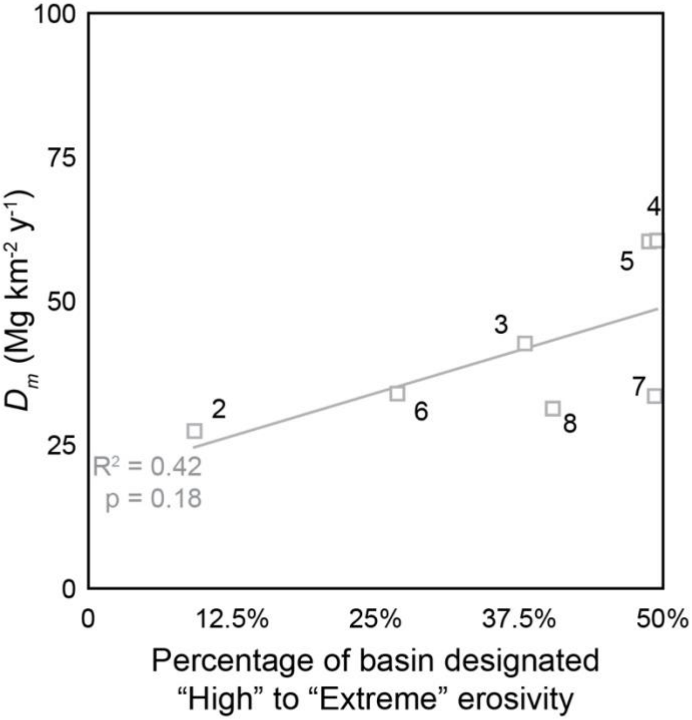

Figure 8: ^{10}Be$_m$/^{9}Be$_{reac}$-based denudation rates, D_m, (gray squares) from tributary basins measured at George River are related to the percentage of the basin that is classified as "High," "Very High," or "Extreme" Erosivity (Kidd et al., 2014, 2015), though this relationship is not significant (p = 0.18). The basins with the highest denudation rates are those with histories of intensive mining and/or recent forestry, both of which disturb topsoils.

Any process-based explanation for the correlation of erosion rates with elevation requires that we consider how relevant geomorphic and geochemical processes vary across the George River basin. Climatic data collected from stations in and near the George River basin indicate that both mean annual temperature and mean annual precipitation are strongly correlated with elevation (Fig. 3). At higher elevations, rocks are experiencing lower temperatures more frequently and receive more precipitation than lower elevations, increasing the potential for both mechanical (frost cracking) and chemical weathering (dissolution). Frost cracking rates are greatest in rocks where mean annual temperature is above freezing (which is the case for all of the George River basin) but temperatures go below freezing both long and frequently enough to crack rocks, which is also the case across much of the basin (Delunel et al., 2010; Hales and Roering, 2007). In the George River basin, the only temperature-related metric that correlates with elevation is mean annual temperature, in contrast to, for example, the time spent below freezing, likely because temperature inversions, with cold air drainage to lower elevation valleys, are common (Webb et al., 2018, 2020). Additionally, the underlying mechanics that lead to rock fracturing in the first place have been demonstrated to be strongly linked to climate and the availability of water (Eppes and Keanini, 2017; Eppes et al., 2018). While water is plentiful across the George River basin, we see that ε is greater at higher elevations where rainfall is also greater, facilitating faster breakdown of rock.

Mean annual precipitation at meteorology stations in the George River basin varies less (2.7-fold) from low to high elevations (681–1,836 mm y^{-1}; Fig. 3) than ε (4.8–24.5 mm ky^{-1}; a 5.1-fold difference; Table 4). The elevation-induced precipitation and erosion rate gradients we observe are consistent with suggestions made at regional and global scales that the relationship between slope and erosion becomes secondary to precipitation in low-slope, low-elevation, post-tectonic settings (Henck et al., 2011; Mishra et al., 2018). We note that Mishra et al. (2018) also suggest that at the global scale, the erosional effects of increased of precipitation may be balanced by increased vegetation cover, which serves to stymy erosion. However, the George River basin is densely vegetated throughout, and forests are no more prevalent at higher than lower elevations in our field area. We propose that in the George River basin, ε is related to elevation in large part because precipitation is strongly correlated with elevation. This interpretation seems to hold true for bedrock outcrops, the erosion rates of which are most-closely correlated to mean annual rainfall in aseismic landscapes; however, basin-wide erosion rates in aseismic areas globally remain more strongly correlated to mean basin slope and subsequently to elevation and climate-related processes (Portenga and Bierman, 2011), which stands in contrast to the relationship we observe here between elevation and ε.

The very strong relationship between elevation, climate (both mean annual rainfall and temperature), and ε would likely not have emerged had our ^{10}Be$_i$ samples been affected by clast attrition (Carretier et al., 2009), deep-seated landslides (Aguilar et al., 2014; Gonzalez et al., 2016; Puchol et al., 2014), or intensive erosion associated with mining, forestry, or agriculture (Barreto et al., 2014; Neilson et al., 2017). Even intensive tin mining, which supplied >10^6 m^3 to the George River over the last two centuries (Knighton, 1991) seems not to have had a long-lasting diluting effect on ^{10}Be$_i$ in sampled stream sediment. It is possible that mining efforts, especially sluice mining, did not lead to ^{10}Be$_i$ dilution because of the homogenizing effect of ^{10}Be$_i$ in bioturbated soils (Brown et al., 1995) or because the size of the George River basin is large enough to buffer the effects of mining efforts in a similar way that large catchments may buffer the effects of landslide material (Niemi et al., 2005; Yanites et al., 2009). It is also possible that mining activity did lead to $^{10}Be_i$ dilution, but concentrations have normalized along with bedload characteristics (Knighton, 1991), similar to the rapid, two-year recovery of $^{10}Be_i$ concentrations following storm-triggered landslides in Puerto Rico (Grande et al., 2021).

Overall, the close relationship between $^{10}Be_i$ erosion rates and climate across the George River basin demonstrates that $^{10}Be_i$ erosion rates reflect background, geologically-meaningful rates of landscape evolution on millennial timescales, even in areas with long histories of intensive human land-use (e.g. Barreto et al., 2014; Rosenkranz et al., 2018; Vanacker et al., 2007). Secondarily, that higher values of ε are observed where there is more rainfall and are colder temperatures suggests that more sediment is being generated in the western portion of the catchment. There, larger volumes of rainfall and colder temperatures facilitate the generation, erosion, entrainment, and delivery of more sediment to trunk channels than in the eastern portion of the catchment.

Since pre-disturbance stream flow and bedload conditions were re-established by the 1990s (Knighton, 1991), it appears the greatest risk of enhanced sediment flux from the George River to Georges Bay in the future comes from land-use changes involving the widespread disturbance of surficial soils, such as through forestry (Wilson, 1999). The percentage of land used for production forestry in native environments has been decreasing throughout the 21st century (Fig. 4), and while some of this land use is being supplanted by Conservation and Protected Native Land Cover, which could buffer the effects of widespread erosion, much is being replaced by grazing and agriculture, which would likely increase erosion, particularly in the headwater catchments where geological erosion rates are naturally higher (Fig. 4). Given recent land-use trends, the $^{10}Be_i$ erosion rates presented here provide a useful benchmark level of sediment delivery to the George River, Georges Bay, and other fluvial systems in northeast Tasmania that share topographic and geologic characteristics similar to those of the George River basin.

5.2 Considerations of ε for trunk channel versus tributary sites

The mass leaving the tributaries (10,511 ± 394 Mg y^{-1}) is about the same as the mass passing through TG-1 (10,286 ± 859 Mg y^{-1}) and the mass of sediment leaving TG-9 (9,555 ± 817 Mg y^{-1}). We infer from these data that the $^{10}Be_i$ measured at TG-1 and TG-9 trunk channel locations is dominated by mass loss in the higher-elevation tributary basins with minimal sediment input from the George River valley bottoms. Similar interpretations have been made elsewhere, albeit in much larger river basins (i.e., Wittmann et al. 2009, 2011, 2016). Given these similarities, we average ε from the two trunk channel sites to produce a nominal average erosion rate for the George River basin as a whole (24.1 ± 1.4 Mg km^{-2} y^{-1}; or 8.9 ± 0.5 mm $ky^{-1}$when dividing ε by rock density, $\rho = 2.7$ g cm^{-3}), which is of similar magnitude to the average erosion rate of catchments draining the eastern flanks of the Great Dividing Range along the southeastern passive margin of mainland Australia (11.6 mm ky^{-1}; Fig. 9; Codilean et al., 2021). Average ε from the George River basin is most consistent with erosion of basins across the Bass Strait, which share similar topographic characteristics and geological histories as the

George River basin (Codilean et al., 2021). The similarity between the geology, topography, and climate of newly-sampled basins and derived $^{10}Be_i$ erosion rates in Tasmania from this study and those from southeast mainland Australia supports the notion that evolution of landscapes that share similar climatic, topographic, and geologic characteristics is similar.

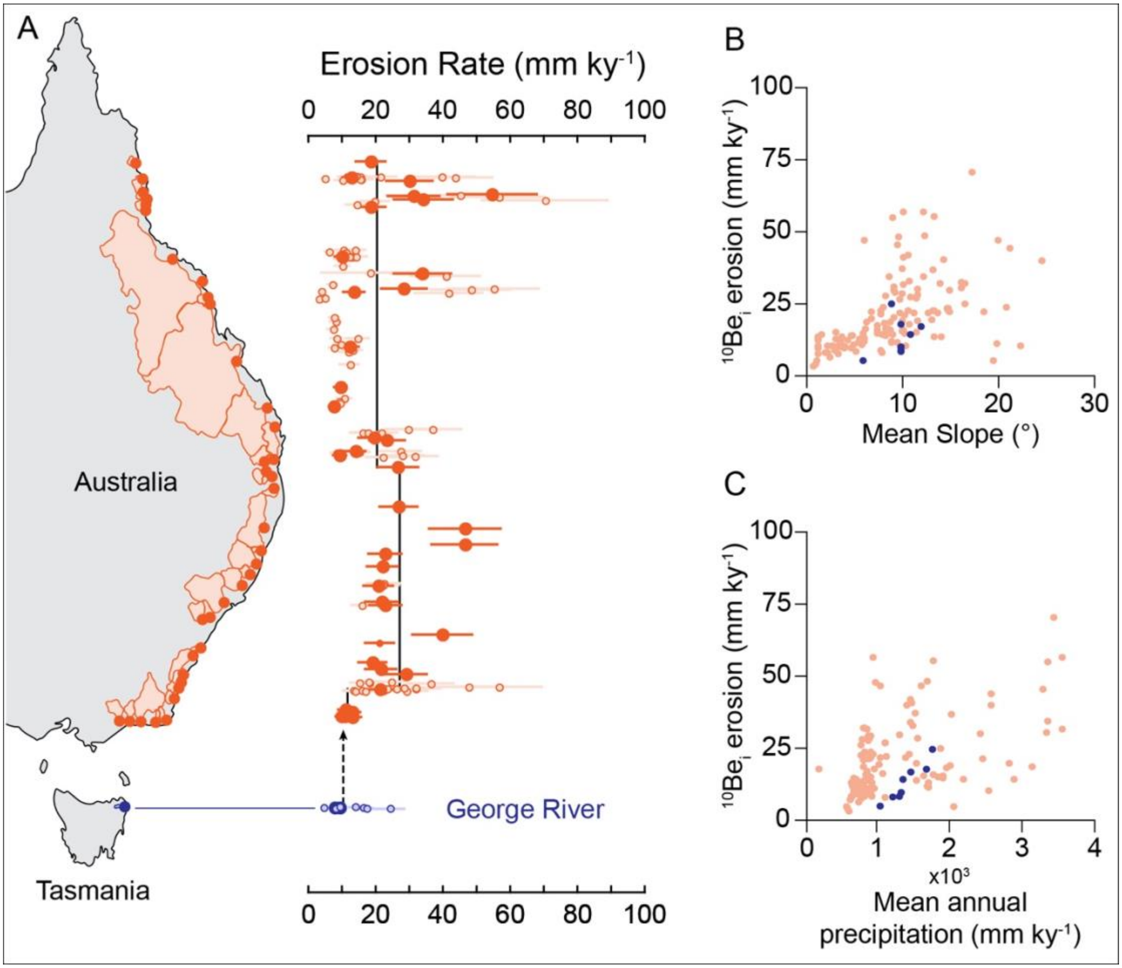

Figure 9: A. Map of river basins draining east off the Great Australian Escarpment, where $^{10}Be_i$ erosion rate data are available; adapted from Codilean et al. (2021). Filled circles are trunk streams and open circles are tributaries. Orange data include previously-published data (Codilean et al., 2021; Croke et al., 2015; Fülöp et al., 2020; Godard et al., 2019; Nichols et al., 2014; Tomkins et al., 2007). Blue data are new data presented in this study from the George River basin, Tasmania. The average $^{10}Be_i$ erosion rates from the George River (8.9 mm ky^{-1}) is consistent with erosion rates from southeast mainland Australia (average 11.6 mm ky^{-1}; Codilean et al., 2021). B. Comparison of $^{10}Be_i$ erosion rates from the George River basin (blue circles) and the eastern flanks of the Great Australian Escarpment (orange circles) to basin average slope. C. Comparison of $^{10}Be_i$ erosion rates from the George River basin (blue circles) and the eastern flanks of the Great Australian Escarpment (orange circles) to mean annual precipitation; in this comparison, mean annual precipitation for George River samples comes from the elevation scaling for measured rainfall at meteorological gauging stations (Figs. 2, 3, Table 1) whereas Codilean et al. (2021) summarize precipitation data for mainland basins from the WorldClim database (Fick and Hijamans, 2017).

5.3 Comparing $^{10}Be_i$-based erosion rates and $^{10}Be_m$-based denudation rates

Once delivered to Earth's surface in temperate regions, $^{10}Be_m$ concentrates in uppermost soil horizons (Graly et al., 2010; Willenbring and von Blanckenburg, 2010). This behaviour differs from that of $^{10}Be_i$, the concentration of which remains homogenous in well-mixed, bioturbated soils for millennia (Jungers et al., 2009). Thus, any disturbance of large volumes of topsoil (i.e., agriculture, forestry, wildfire erosion, or mining activities) strips material with the highest concentrations of $^{10}Be_m$ and introduces that material into streams, a process similar to that identified following early land-use changes and deforestation in the Chesapeake Bay and San Francisco Bay (Portenga et al., 2019; Valette-Silver et al., 1986; van Geen et al., 1999). In contrast, the strong relationship between $^{10}Be_i$ erosion rates and elevation, and thus both precipitation and temperature, across the George River basin (Fig. 6) suggests that $^{10}Be_i$ erosion rates, ε, are unaffected by land use.

Calculated values of D_m do not replicate ε (Fig. 7), nor does D_m replicate the spatial patterns or yield the same relationships with topographic and climate parameters that we observe with ε in the small, geologically-homogeneous landscape of the George River basin (e.g., Fig. 6). We know that decades-old historical mining activities and historical bushfires in the George River were restricted to lower catchment areas and tributaries where measurements of D_m are highest (Figs. 4, 8). Additionally, we infer from the moderate correlation observed between D_m and the percent of tributary basins classified as "High" to "Extreme" Erosivity ($R^2 = 0.33$; Fig. 8; Kidd et al., 2014, 2015) that $^{10}Be_m/^{9}Be_{reac}$-derived denudation rates appear to be sensitive to recent land-use practices that disturb soils. The highest denudation rates, D_m, we measured are those from basins with past histories of intense surface disruption through mining and forestry (i.e., TG-4, TG-5).

The similarity of D_m and ε for the entire George River basin, however—within a factor of 2 (Fig. 7)—provides general support for the hypothesis that $^{10}Be_m/^{9}Be_{reac}$-based denudation rates more-closely resemble $^{10}Be_i$-based erosion rates in small river basins where geological heterogeneity is minimized. This observed similarity between D_m and ε supports the continued exploration and application of $^{10}Be_m/^{9}Be_{reac}$ denudation rates in geomorphological studies. However, data presented here suggest that this method should be used with caution in landscapes with recent soil disturbance (Dannhaus et al., 2017; Deng et al., 2020; Portenga et al., 2019; Rahaman et al., 2017; Wittmann et al., 2012, 2015).

5.4 Where does the dissolved load originate in the George River basin?

If chemical weathering occurs primarily in the uppermost meters of the landscape, where most $^{10}Be_i$ is produced, then the erosion rate, ε, we calculate represents landscape mass loss over time—a combination of physical and chemical mass loss. We could then partition ε along the trunk channel at the mouth of the George River basin (TG-9 = 22.4 Mg km^{-2} y^{-1}) into mass flux removed in dissolved load (10.3 Mg km^{-2} y^{-1}) and the remainder, mass flux removed as solid sediment (12.1 Mg km^{-2} y^{-1}). Of the sediment mass flux, it appears that 4.3 Mg km^{-2} y^{-1} is transported as suspended load and 7.8 Mg km^{-2} y^{-1} is bedload. Our measure of ε at TG-9 is ~40% lower than the $^{10}Be_m/^{9}Be_{reac}$ measure of denudation at this site (38.4 Mg km^{-2} y^{-1}), which if the assumptions of the method are met, represents total physical and chemical mass loss. Taken at face value, either D_m overestimates total mass loss from the George basin at TG-9 or ε underestimates denudation, both by 40%. Coincidentally, an independent measure of weathering at TG-9, based on $^{9}Be_{min}$ and $^{9}Be_{reac}$ data (equation 9 in Wittmann et al., 2015) suggests that there is a ~40% weathering degree at this site, which suggests that ε underestimates denudation.

If the majority of chemical weathering occurs below the penetration depth of most cosmic rays (< 2 m), then the chemical denudation and physical mass loss are at least in part and perhaps wholly disconnected. In this case, ε (TG-9 = 22.4 Mg km^{-2} y^{-1}) would need to be summed with the chemical mass flux (10.3 Mg km^{-2} y^{-1}) and together (30.7 Mg km^{-2} y^{-1}), they would estimate the total mass loss from the landscape. The presence of bedrock outcrops in some of the George River basin channels suggests that regolith thickness is limited in places and in that case, $^{10}Be_i$ measurements incorporate much of the chemical mass loss from the basin. However, the few boreholes that extend to unweathered bedrock (n = 3; Fig. 2; Table 1) clearly indicate that regolith is deeper in some parts of the catchment. With the paucity of available data, we cannot determine how much of the dissolved load is coming from below the penetration depth of cosmic-ray neutrons but it could be significant.

Summing ε and the dissolved load (30.7 Mg km^{-2} y^{-1}) results in a total mass loss more consistent with that suggested by $^{10}Be_{met}/^{9}Be_{reac}$-based denudation rate at TG-9, D_m = 38.4 Mg km^{-2} y^{-1}. Yet, the $^{10}Be_{met}/^{9}Be_{reac}$-based denudation rates appear to have little correlation with landscape scale metrics—and are highest in basins with known histories of intensive land-use disturbance and erosivity (Figs. 2, 8)—making it uncertain they still reflect the rate of geomorphic processes controlling mass loss over time. In contrast, ε is well-correlated to elevation and thus temperature and precipitation. With the data set presented here, it is not yet possible to know if the balance between physical and chemical mass loss in tributaries is consistent with what we observe at the mouth of George River.

6 Conclusions

The $^{10}Be_i$-based erosion rates we present in this study are the first derived for any river system for Tasmania. In contrast to erosion across the Great Dividing Range on mainland Australia where erosion rates and mean basin slope are closely linked, erosion in the George River basin has a strong relationship with mean basin elevation, and thus with mean annual precipitation and mean annual temperature, which are both strongly correlated with elevation. The average $^{10}Be_i$ erosion rate in the George River basin, 24.1 ± 1.4 Mg km^{-2} y^{-1}, reflects erosion in tributaries to the George River where precipitation is greatest and temperatures are lowest; little sediment is generated in trunk channel valley bottoms. These findings support the notion that precipitation imparts a significant influence on landscape development in low-slope, low-elevation landscapes, which are often located in post-orogenic, passive margin settings. We also suspect that low but positive mean annual temperatures with frequent excursions below zero drives the mechanical breakdown of rock, thereby increasing sediment production in high-elevation basins through frost cracking. Although hillslope erosion associated with mining, agricultural, and forestry land-use practices occurred in the George River basin during the 19th and 20th centuries, $^{10}Be_i$ based erosion rates in the basin appear to reflect pre-disturbance rates of landscape change. Such rates are useful as part of Tasmania's current efforts to re-establish healthy and sustainable ecological conditions in its many estuarine environments, particularly those in northeast Tasmania where estuary tributaries have similar geological and topographic characteristics to those found in the George River basin. $^{10}Be_m/^{9}Be_{reac}$ denudation rates in the central and eastern tributaries of the George River basin generally replicate $^{10}Be_i$-based erosion within a factor of two, but they do not replicate $^{10}Be_i$ erosion data at any sample site, likely owing to intensive topsoil disturbance during decades and centuries of mining, forestry, and agricultural land use. Data from the George River basin support application of $^{10}Be_m/^{9}Be_{reac}$ denudation rates in small, lithologically homogeneous basins with limited amounts of topsoil disturbance.

We would like to acknowledge the Palawa peoples of lutruwita, the traditional custodians of the lands on which this work was completed.

Data Availability

All maps were created by EWP; data within maps (e.g. DEMs, geology, etc.) is properly cited. All data used in this study and all data needed to reproduce our findings and the equations used to calculate $^{10}Be_i$ erosion rates and $^{10}Be_m/^{9}Be_{reac}$ denudation rates are presented in Tables 1–6. Mean annual precipitation and geological borehole data were gathered from online databases supported by the Australian Bureau of Meteorology (Rainfall: http://www.bom.gov.au/climate/data/; borehole: http://www.bom.gov.au/water/groundwater/explorer/index.shtml). Mean annual temperature data come from the State of Tasmania Air Temperature Logger Recording Database (© 2018 State of Tasmania), accessed through personal communication. Water quality data for the water intake station in St. Helens was provided by TasWater (pers. comm. John Fawcett).

Author Contribution

The conceptual analysis of the data presented in this paper comes from LAV's Undergraduate Honors Thesis (2020) at Eastern Michigan University. EWP, PRB, and AHS contributed to post-thesis manuscript revisions, data analysis, and figure drafting. Samples and the $^{10}Be_i$ data presented here were collected and facilitated by PRB and ECL in 2008. ^{9}Be and $^{10}Be_m$ data were first presented in Sophie E. Greene's Master's Thesis (2016) at the University of Vermont; SEG declined a request to participate in the writing and publication of this paper. AHS completed chemical weathering calculations. AJH verified Lawrence Livermore National Laboratory's measurement of beryllium at the Center for Accelerator Mass Spectrometry in 2009. This work was performed in part under the auspices of the U.S. Department of Energy by Lawrence Livermore National Laboratory under Contract DE-AC52- 07NA27344. This is LLNL-JRNL-825534.

References

ABARES, 2016, The Australian Land Use and Management Classification Version 8: Australian Bureau of Agricultural and Resource Economics and Sciences, https://www.agriculture.gov.au/abares/aclump/land-use/alum-classification.

Adams, B. A., and Ehlers, T., 2017, Deciphering topographic signals of glaciation and rock uplift in an active orogen: A case study from the Olympic Mountains, USA: Earth Surface Processes and Landforms, v. 42, no. 11, p. 1680-1692.

Aguilar, G., Carretier, S., Regard, V., Vassallo, R., Riquelme, R., and Martinod, J., 2014, Grain size-dependent 10Be concentrations in alluvial stream sediment of the Huasco Valley, a semi-arid Andes region: Quaternary Geochronology, v. 19, p. 163-172.

Aldahan, A., Haiping, Y., and Possnert, G., 1999. Distribution of beryllium between solution and minerals (biotite and albite) under atmospheric conditions and variable pH: Chemical Geology, v. 156, no. 1–4, p. 209–229.

Balco, G., Stone, J. O., Lifton, N. A., and Dunai, T. J., 2008, A complete and easily accessible means of calculating surface exposure ages or erosion rates from 10Be and 26Al measurements: Quaternary Geochronology, v. 3, no. 3, p. 174-195.

Barreto, H. N., Varajão, C. A. C., Braucher, R., Bourlès, D. L., Salgado, A. A. R., and Varajão, A. F. D. C., 2014, The impact of diamond extraction on natural denudation rates in the Diamantina Plateau (Minas Gerais, Brazil): Journal of South American Earth Sciences, v. 56, p. 357-364.

Barrows, T. T., Stone, J. O., Fifield, L. K., and Cresswell, R. G., 2001, Late Pleistocene Glaciation of the Kosciuszko Massif, Snowy Mountains, Australia: Quaternary Research, v. 55, no. 2, p. 179-189.

-, 2002, The timing of the Last Glacial Maximum in Australia: Quaternary Science Reviews, v. 21, no. 1, p. 159-173.

Batley, G., Crawford, C., Moore, M., McNeil, J., Reid, J., Koehnken, L., and Ramsay, J., 2010, Report of the George River Water Quality Panel.

Belmont, P., Pazzaglia, F., and Gosse, J. C., 2007, Cosmogenic 10Be as a tracer for hillslope and channel sediment dynamics in the Clearwater River, western Washington State: Earth and Planetary Science Letters, v. 264, no. 1-2, p. 123-135.

Bierman, P., and Steig, E. J., 1996, Estimating rates of denudation using cosmogenic isotope abundances in sediment: Earth surface processes and landforms, v. 21, no. 2, p. 125-139.

Bleaney, A., Hickey, C. W., Stewart, M., Scammell, M., and Senjen, R., 2015, Preliminary investigations of toxicity in the Georges Bay catchment, Tasmania, Australia: International Journal of Environmental Studies, v. 72, no. 1, p. 1-23.

BoM, 2015, Australian Groundwater Explorer: Australia Bureau of Meteorology, http://www.bom.gov.au/water/groundwater/explorer.index.shtml.

BoM, 2021, Climate Data Online: Australia Bureau of Meteorology, http://www.bom.gov.au/climate/data/.

Braucher, R., Brown, E., Bourlès, D., and Colin, F., 2003, In situ produced 10Be measurements at great depths: implications for production rates by fast muons: Earth and Planetary Science Letters, v. 211, no. 3-4, p. 251-258.

Brown, E. T., Stallard, R. F., Larsen, M. C., Raisbeck, G. M., and Yiou, F., 1995, Denudation rates determined from the accumulation of in situ-produced 10Be in the Luquillo Experimental Forest, Puerto Rico: Earth and Planetary Science Letters, v. 129, no. 1-4, p. 193-202.

Brown, L., Pavich, M. J., Hickman, R. E., Klein, J., and Middleton, R., 1988, Erosion of the eastern United States observed with 10Be: Earth Surface Processes and Landforms, v. 13, no. 5, p. 441-457.

Carretier, S., Regard, V., and Soual, C., 2009, Theoretical cosmogenic nuclide concentration in river bed load clasts: Does it depend on clast size?: Quaternary Geochronology, v. 4, no. 2, p. 108-123.

Carretier, S., Tolorza, V., Regard, V., Aguilar, G., Bermúdez, M. A., Martinod, J., Guyot, J. L., Hérail, G., and Riquelme, R., 2018, Review of erosion dynamics along the major NS climatic gradient in Chile and perspectives: Geomorphology, v. 300, p. 45-68.

Carretier, S., Tolorza, V., Rodríguez, M., Pepin, E., Aguilar, G., Regard, V., Martinod, J., Riquelme, R., Bonnet, S., and Brichau, S., 2015, Erosion in the Chilean Andes between 27 S and 39 S: tectonic, climatic and geomorphic control: Geological Society, London, Special Publications, v. 399, no. 1, p. 401-418.

Cheetham, M. D., and Martin, J. C., 2018, Hope for the best, plan for the worst: Managing sediment input in the upper catchment whilst preparing for avulsion at the mouth, 9th Australian Stream Management Conference: Hobart, Tasmania, Australia, p. 8.

Codilean, A. T., Fülöp, R.-H., Munack, H., Wilcken, K. M., Cohen, T. J., Rood, D. H., Fink, D., Bartley, R., Croke, J., and Fifield, L., 2021, Controls on denudation along the East Australian continental margin: Earth-Science Reviews, p. 103543.

Codilean, A. T., Munack, H., Cohen, T. J., Saktura, W. M., Gray, A., and Mudd, S. M., 2018, OCTOPUS: an open cosmogenic isotope and luminescence database: Earth System Science Data, v. 10, no. 4, p. 2123-2139.

Colhoun, E. A., 2002, Periglacial landforms and deposits of Tasmania : Periglacial and Permafrost Research in the Southern Hemisphere: South African Journal of Science, v. 98, no. 1, p. 55-63.

Corbett, L. B., Bierman, P. R., and Rood, D. H., 2016, An approach for optimizing in situ cosmogenic 10Be sample preparation: Quaternary Geochronology, v. 33, p. 24-34.

Cosgrove, R., 1995, Late Pleistocene behavioural variation and time trends: the case from Tasmania: Archaeology in Oceania, v. 30, no. 3, p. 83-104.

Cosgrove, R., Allen, J., and Marshall, B., 1990, Palaeo-ecology and Pleistocene human occupation in south central Tasmania: Antiquity, v. 64, no. 242, p. 59-78.

Crawford, C., and White, C., 2005, Establishment of an integrated water quality monitoring framework for Georges Bay.

Croke, J., Bartley, R., Chappell, J., Austin, J. M., Fifield, K., Tims, S. G., Thompson, C. J., and Furuichi, T., 2015, 10Be-derived denudation rates from the Burdekin catchment: The largest contributor of sediment to the Great Barrier Reef: Geomorphology, v. 241, p. 122-134.

Crowder, E., Rawlinson, N., Pilia, S., Cornwell, D. G., and Reading, A. M., 2019, Transdimensional ambient noise tomography of Bass Strait, southeast Australia, reveals the sedimentary basin and deep crustal structure beneath a failed continental rift: Geophysical Journal International, v. 217, no. 2, p. 970-987.

Dannhaus, N., Wittmann, H., Krám, P., Christl, M., and von Blanckenburg, F., 2018, Catchment-wide weathering and erosion rates of mafic, ultramafic, and granitic rock from cosmogenic meteoric 10Be/9Be ratios: Geochimica et Cosmochimica Acta, v. 222, p. 618-641.

Delunel, R., Schlunegger, F., Valla, P. G., Dixon, J., Glotzbach, C., Hippe, K., Kober, F., Molliex, S., Norton, K. P., Salcher, B., Wittmann, H., Akçar, N., and Christl, M., 2020, Late-Pleistocene catchment-wide denudation patterns across the European Alps: Earth-Science Reviews, v. 211, p. 103407.

Delunel, R., van der Beek, P. A., Carcaillet, J., Bourlès, D. L., and Valla, P. G., 2010, Frost-cracking control on catchment denudation rates: Insights from in situ produced 10Be concentrations in stream sediments (Ecrins–Pelvoux massif, French Western Alps): Earth and Planetary Science Letters, v. 293, no. 1-2, p. 72-83.

Deng, K., Yang, S., von Blanckenburg, F., and Wittmann, H., 2020, Denudation Rate Changes Along a Fast-Eroding Mountainous River With Slate Headwaters in Taiwan From 10Be (Meteoric)/9Be Ratios: Journal of Geophysical Research: Earth Surface, v. 125, no. 2, p. e2019JF005251.

DPIPWE, 2021, Water Information for George River at St. Helens Water Supply, Site ID 2205, Water Information Tasmania Web Portal, Tasmanian Department of Primary Industries, Parks, Water, and Environment, https://portal.wrt.tas.gov.au/Data/Location/Summary/Location/2205-1/Interval/Latest (accessed, 22 September 2021).

DPIPWE, 2021, Water Information for Ransom River at Sweets Hill, Site ID 2217, Water Information Tasmania Web Portal, Tasmanian Department of Primary Industries, Parks, Water, and Environment, https://portal.wrt.tas.gov.au/Data/Location/Summary/Location/2217-1/Interval/Latest (accessed, 22 September 2021).

Dethier, D. P., Ouimet, W., Bierman, P. R., Rood, D. H., and Balco, G., 2014, Basins and bedrock: Spatial variation in 10Be erosion rates and increasing relief in the southern Rocky Mountains, USA: Geology, v. 42, no. 2, p. 167-170.

Eppes, M.-C. and Keanini, R., 2017. Mechanical weathering and rock erosion by climate-dependent critical subcritical cracking: Review of Geophysics, v. 55, no. 2, p. 470–508.

Eppes, M.-C., Hancock, G. S., Chen, X., Arey, J., Dewers, ,T., Huettenmoser, J., Kiessling, S., Moser, F., Tannu, N., Weiserbs, B., and Whitten, J., 2018. Rates of subcritical cracking and long-term rock erosion: Geology, v. 46, no. 11, p. 951–954.

Etheridge, M. A., Branson, J. C., and Stuart-Smith, P. G., 1987, The Bass, Gippsland and Otway basins, southeast Australia: A branched rift system formed by continental extension: Sedimentary Basins and Basin-forming Mechanisms, v. Memoir 12, p. 147-162.

Fellin, M. G., Chen, C.-Y., Willett, S. D., Christl, M., and Chen, Y.-G., 2017, Erosion rates across space and timescales from a multi-proxy study of rivers of eastern Taiwan: Global and Planetary Change, v. 157, p. 174-193.

Ferrier, K. L., Kirchner, J. W., and Finkel, R. C., 2005, Erosion rates over millennial and decadal timescales at Caspar Creek and Redwood Creek, northern California Coast Ranges: Earth Surface Processes and Landforms: The Journal of the British Geomorphological Research Group, v. 30, no. 8, p. 1025-1038.

Fick, S. E., and Hijmans, R. J., 2017, WorldClim 2: new 1-km spatial resolution climate surfaces for global land areas: International Journal of Climatology, v. 37, no. 12, p. 4302-4315.

Foster, D. A., and Gray, D. R., 2000, Evolution and Structure of the Lachlan Fold Belt (Orogen) of Eastern Australia: Annual Review of Earth and Planetary Sciences, v. 28, no. 1, p. 47-80.

Fülöp, R.-H., Codilean, A. T., Wilcken, K. M., Cohen, T. J., Fink, D., Smith, A. M., Yang, B., Levchenko, V. A., Wacker, L., Marx, S. K., Stromsoe, N., Fujioka, T., and Dunai, T. J., 2020, Million-year lag times in a post-orogenic sediment conveyor: Science Advances, v. 6, no. 25, p. eaaz8845.

Gaina, C., Müller, D. R., Royer, J.-Y., Stock, J., Hardebeck, J., and Symonds, P., 1998, The tectonic history of the Tasman Sea: A puzzle with 13 pieces: Journal of Geophysical Research: Solid Earth, v. 103, no. B6, p. 12413-12433.

Gallant, J., Wilson, N., Dowling, T., Read, A., and Inskeep, C., 2011, SRTM-derived 1 Second Digital Elevation Models Version 1.0. Record 1: Geoscience Australia, Canberra, ACT, Australia.

Gee, R. D., and Groves, D. I., 1971, Structural features and mode of emplacement of part of the blue tier batholith in Northeast Tasmania: Journal of the Geological Society of Australia, v. 18, no. 1, p. 41-55.

Godard, V., Dosseto, A., Fleury, J., Bellier, O., and Siame, L., 2019, Transient landscape dynamics across the Southeastern Australian Escarpment: Earth and Planetary Science Letters, v. 506, p. 397-406.

Gonzalez, V. S., Bierman, P. R., Nichols, K. K., and Rood, D. H., 2016, Long-term erosion rates of Panamanian drainage basins determined using in situ 10Be: Geomorphology, v. 275, p. 1-15.

Gosse, J. C., and Phillips, F. M., 2001, Terrestrial in situ cosmogenic nuclides: theory and application: Quaternary Science Reviews, v. 20, no. 14, p. 1475-1560.

Graly, J. A., Bierman, P. R., Reusser, L. J., and Pavich, M. J., 2010, Meteoric 10Be in soil profiles – A global meta-analysis: Geochimica et Cosmochimica Acta, v. 74, no. 23, p. 6814-6829.

Graly, J. A., Reusser, L. J., and Bierman, P. R., 2011, Short and long-term delivery rates of meteoric 10Be to terrestrial soils: Earth and Planetary Science Letters, v. 302, no. 3, p. 329-336.

Grande, A., Schmidt, A. H., Bierman, P. R., Corbett, L. B., López-Lloreda, C., Willenbring, J., McDowell, W. H., and Caffee, M. W., 2021, Landslides, hurricanes, and sediment sourcing impact basin-scale erosion estimates in Luquillo, Puerto Rico: Earth and Planetary Science Letters, v. 562, p. 116821.

Granger, D. E., Kirchner, J. W., and Finkel, R., 1996, Spatially averaged long-term erosion rates measured from in situ-produced cosmogenic nuclides in alluvial sediment: The Journal of Geology, v. 104, no. 3, p. 249-257.

Gray, D. R., and Foster, D. A., 2004, Tectonic evolution of the Lachlan Orogen, southeast Australia: Historical review, data synthesis and modern perspectives: Australian Journal of Earth Sciences, v. 51, no. 6, p. 773-817.

Greene, E. S., 2016, Comparing meteoric 10Be, in situ 10Be, and native 9Be across a diverse set of watersheds, Master’s Thesis, Geology Department, University of Vermont, Burlington, VT, United States, 118 p.

Griffiths, J. R., 1971, Continental margin tectonics and the evolution of south-east Australia: The APPEA Journal, v. 11, no. 1, p. 75-79.

Gunn, P. J., 1975, Mesozoic-Cainozoic Tectonics and Igneous Activity: Southeastern Australia: Journal of the Geological Society of Australia, v. 22, no. 2, p. 215-221.

Hales, T. C. and Roering, J. J., 2006. Climatic controls on frost cracking and implications for the evolution of bedrock landscapes: Journal of Geophysical Research, v. 11, F02033.

Harel, M.-A., Mudd, S., and Attal, M., 2016, Global analysis of the stream power law parameters based on worldwide 10Be denudation rates: Geomorphology, v. 268, p. 184-196.

Harrison, E. J., Willenbring, J. K., and Brocard, G. Y., 2021, Quaternary record of terrestrial environmental change in response to climatic forcing and anthropogenic perturbations, in Puerto Rico: Quaternary Science Reviews, v. 253, p. 106770.

Hayes, D. E., and Ringis, J., 1973, Seafloor Spreading in the Tasman Sea: Nature, v. 243, no. 5408, p. 454-458.

Heikkilä, U., and von Blanckenburg, F., 2015, The global distribution of Holocene meteoric 10Be fluxes from atmospheric models. Distribution maps for terrestrial Earth’s surface applications, GFZ Data Services, doi.10.5880/GFZ.3.4.2015.001

Heisinger, B., Niedermayer, M., Hartmann, F., Korschinek, G., Nolte, E., Morteani, G., Neumaier, S., Petitjean, C., Kubik, P., and Synal, A., 1997, In-situ production of radionuclides at great depths: Nuclear Instruments and Methods in Physics Research Section B: Beam Interactions with Materials and Atoms, v. 123, no. 1-4, p. 341-346.

Helz, G. R., and Valette-Silver, N., 1992, Beryllium-10 in Chesapeake Bay sediments: An indicator of sediment provenance: Estuarine, Coastal and Shelf Science, v. 34, no. 5, p. 459-469.

Henck, A. C., Huntington, K. W., and Hallet, B., 2011. Spatial controls on erosion in the Three Rivers Region, southwest China: Earth and Planetary Science Letters, v. 303, p. 71–83.

Higgins, N. C., Solomon, M., and Varne, R., 1985, The genesis of the Blue Tier Batholith, northeastern Tasmania, Australia: Lithos, v. 18, p. 129-149.

Huffman, G., Pendergrass, J., and Angeline & National Center for Atmospheric Research Staff (Eds.), 2021. The Climate Data Guide: TRMM: Tropical Rainfall Measuring Mission: Last modified 20 Mar 2021. Retrieved from https://climatedataguide.ucar.edu/climate-data/trmm-tropical-rainfall-measuring-mission.

Jerie, K., Houshold, I., and Peters, D., 2003, Tasmania's river geomorphology: stream character and regional analysis: Nature Conservation Branch, DPIWE.

Jones, P. J., Williamson, G. J., Bowman, D. M. J. S., Lefroy, E. C., 2019, Mapping Tasmania's cultural landscapes: Using habitat suitability modelling of archaeological sites as a landscape history tool: Journal of Biogeography, v. 46, no. 11, p. 2570-2582.

Jungers, M. C., Bierman, P. R., Matmon, A., Nichols, K., Larsen, J., and Finkel, R., 2009, Tracing hillslope sediment production and transport with in situ and meteoric ^{10}Be: Journal of Geophysical Research, v. 114, F04020.

Kidd, D., Malone, B., McBratney, A., Minasny, B., Odgers, N., Webb, M., and Searle, R., 2014, A new digital soil resource for Tasmania, Australia, in Proceedings 20th World Congress of Soil Science, p. 612-613.

Kidd, D., Webb, M., Malone, B., Minasny, B., and McBratney, A., 2015, 80-metre resolution 3D soil attribute maps for Tasmania, Australia: Soil Research, doi. 10.1071/SR14268.

Knighton, A., 1991, Channel bed adjustment along mine-affected rivers of northeast Tasmania: Geomorphology, v. 4, no. 3-4, p. 205-219.

Koehnken, L., 2001, North-east rivers environmental review: A review of Tasmanian environmental quality data to 2001: Supervising Scientist Report 168, Australian Government Department of Agriculture, Water and the Environment, pp. 64.

Kohl, C. P., and Nishiizumi, K., 1992, Chemical isolation of quartz for measurement of in-situ -produced cosmogenic nuclides: Geochimica et Cosmochimica Acta, v. 56, no. 9, p. 3583-3587.

Kottek, M., Grieser, J., Beck, C., Rudolf, B., and Rubel, F., 2006, World map of the Köppen-Geiger climate classification updated: Meteorologische Zeitschrift, v. 15, no. 3, p. 259-263.

Kragt, M. E., and Newham, L. T., 2009, Developing a water-quality model for the George catchment, Tasmania: Landscape Logic.

Lal, D., 1991, Cosmic ray labeling of erosion surfaces: in situ nuclide production rates and erosion models: Earth and Planetary Science Letters, v. 104, no. 2-4, p. 424-439.

Land-Tasmania, 2020, Fire History [of Tasmania]: Tasmania Department of Primary Industries, Water and Environment, Hobart, Tasmania, Australia, https://www.thelist.tas.gov.au/app/content/data/geo-meta-data-record?detailRecordUID=b94d4388-995d-416a-9844-a39de2798bed.

Lanyon, R., Varne, R., and Crawford, A. J., 1993, Tasmanian Tertiary basalts, the Balleny plume, and opening of the Tasman Sea (southwest Pacific Ocean): Geology, v. 21, no. 6, p. 555-558.

Mackintosh, A. N., Barrows, T. T., Colhoun, E. A., and Fifield, L. K., 2006, Exposure dating and glacial reconstruction at Mt. Field, Tasmania, Australia, identifies MIS 3 and MIS 2 glacial advances and climatic variability: Journal of Quaternary Science, v. 21, no. 4, p. 363-376.

Martin, J., and Cheetham, M., 2018, Final Report: Lower George River Investigation: Lower George Riverworks Trust.

Masarik, J., and Beer, J., 2009, An updated simulation of particle fluxes and cosmogenic nuclide production in the Earth's atmosphere: Journal of Geophysical Research: Atmospheres, v. 114, no. D11.

Matmon, A., Bierman, P., and Enzel, Y., 2002, Pattern and tempo of great escarpment erosion: Geology, v. 30, no. 12, p. 1135-1138.

McCarthy, T. S., and Groves, D. I., 1979, The Blue Tier Batholith, Northeastern Tasmania: Contributions to Mineralogy and Petrology, v. 71, no. 2, p. 193-209.

McDougall, I., and van der Lingen, G. J., 1974, Age of the rhyolites of the Lord Howe Rise and the evolution of the southwest Pacific Ocean: Earth and Planetary Science Letters, v. 21, no. 2, p. 117-126.

McIntosh, P. D., Price, D. M., Eberhard, R., and Slee, A. J., 2009, Late Quaternary erosion events in lowland and mid-altitude Tasmania in relation to climate change and first human arrival: Quaternary Science Reviews, v. 28, no. 9, p. 850-872.

McKenny, C., and Shepherd, C., 1999, Ecological flow requirements for the George River: Report Series WRA 99/14, Department of Primary Industries, Water and Environment, Tasmania, pp. 31.

Mishra, A. K., Placzek, C., and Jones, R., 2019, Coupled influence of precipitation and vegetation on millennial-scale erosion rates derived from 10Be: PloS one, v. 14, no. 1, p. e0211325.

Mitchell, I. M., Crawford, C. M., and Rushton, M. J., 2000, Flat oyster (Ostrea angasi) growth and survival rates at Georges Bay, Tasmania (Australia): Aquaculture, v. 191, no. 4, p. 309-321.

Monaghan, M. C., Krishnaswami, S., and Turekian, K. K., 1986, The global-average production rate of10Be: Earth and Planetary Science Letters, v. 76, no. 3, p. 279-287.

Mortimer, N., Campbell, H. J., Tulloch, A. J., King, P. R., Stagpoole, V. M., Wood, R. A., Rattenbury, M. S., Sutherland, R., Adams, C. J., Collot, J., and Seton, M., 2017, Zealandia: Earth’s hidden continent: GSA Today, v. 27, p. 27-35.

Mount, R., Crawford, C., Veal, C., and White, C., 2005, Bringing back the bay: marine habitats and water quality in Georges Bay.

Neilson, T. B., Schmidt, A. H., Bierman, P. R., Rood, D. H., and Sosa Gonzalez, V., 2017, Efficacy of in situ and meteoric 10Be mixing in fluvial sediment collected from small catchments in China: Chemical Geology, v. 471, p. 119-130.

Nichols, K. K., Bierman, P. R., and Rood, D. H., 2014, 10Be constrains the sediment sources and sediment yields to the Great Barrier Reef from the tropical Barron River catchment, Queensland, Australia: Geomorphology, v. 224, p. 102-110.

Niemi, N. A., Oskin, M., Burbank, D. W., Heimsath, A. M., and Gabet, E. J., 2005, Effects of bedrock landslides on cosmogenically determined erosion rates: Earth and Planetary Science Letters, v. 237, no. 3, p. 480-498.

Nishiizumi, K., Imamura, M., Caffee, M. W., Southon, J. R., Finkel, R. C., and McAninch, J., 2007, Absolute calibration of 10Be AMS standards: Nuclear Instruments and Methods in Physics Research Section B: Beam Interactions with Materials and Atoms, v. 258, no. 2, p. 403-413.

Persano, C., Stuart, F. M., Bishop, P., and Barfod, D. N., 2002, Apatite (U–Th)/He age constraints on the development of the Great Escarpment on the southeastern Australian passive margin: Earth and Planetary Science Letters, v. 200, no. 1, p. 79-90.

Portenga, E. W., and Bierman, P. R., 2011, Understanding Earth's eroding surface with 10 Be: GSA Today, v. 21, no. 8, p. 4-10.

Portenga, E. W., Bierman, P. R., Duncan, C., Corbett, L. B., Kehrwald, N. M., and Rood, D. H., 2015, Erosion rates of the Bhutanese Himalaya determined using in situ-produced 10Be: Geomorphology, v. 233, p. 112-126.

Portenga, E. W., Bierman, P. R., Trodick, C. D., Jr., Greene, S. E., DeJong, B. D., Rood, D. H., and Pavich, M. J., 2019, Erosion rates and sediment flux within the Potomac River basin quantified over millennial timescales using beryllium isotopes: GSA Bulletin, v. 131, no. 7-8, p. 1295-1311.

Portenga, E. W., Bishop, P., Rood, D. H., and Bierman, P. R., 2017, Combining bulk sediment OSL and meteoric 10Be fingerprinting techniques to identify gully initiation sites and erosion depths: Journal of Geophysical Research: Earth Surface, v. 122, no. 2, p. 513-527.

Preston, K., 2012, Anchor tin mine, Tasmania: A century of struggle for profitability, Australasian Mining History Association, v. 10, p. 140–159.

Puchol, N., Lavé, J., Lupker, M., Blard, P.-H., Gallo, F., and France-Lanord, C., 2014, Grain-size dependent concentration of cosmogenic 10Be and erosion dynamics in a landslide-dominated Himalayan watershed: Geomorphology, v. 224, p. 55-68.

Rahaman, W., Wittmann, H., and von Blanckenburg, F., 2017, Denudation rates and the degree of chemical weathering in the Ganga River basin from ratios of meteoric cosmogenic 10Be to stable 9Be: Earth and Planetary Science Letters, v. 469, p. 156-169.

Reusser, L., Graly, J., Bierman, P., and Rood, D., 2010a, Calibrating a long-term meteoric 10Be accumulation rate in soil: Geophysical Research Letters, v. 37, no. 19.

Reusser, L. J., and Bierman, P. R., 2010, Using meteoric 10Be to track fluvial sand through the Waipaoa River basin, New Zealand: Geology, v. 38, no. 1, p. 47-50.

Rosenkranz, R., Schildgen, T., Wittmann, H., and Spiegel, C., 2018, Coupling erosion and topographic development in the rainiest place on Earth: Reconstructing the Shillong Plateau uplift history with in-situ cosmogenic 10Be: Earth and Planetary Science Letters, v. 483, p. 39-51.

Schaller, M., Ehlers, T., Lang, K. A., Schmid, M., and Fuentes-Espoz, J., 2018, Addressing the contribution of climate and vegetation cover on hillslope denudation, Chilean Coastal Cordillera (26–38 S): Earth and Planetary Science Letters, v. 489, p. 111-122.

Scherler, D., Bookhagen, B., and Strecker, M. R., 2014, Tectonic control on 10Be-derived erosion rates in the Garhwal Himalaya, India: Journal of Geophysical Research: Earth Surface, v. 119, no. 2, p. 83-105.

Schmidt, A. H., Gonzalez, V. S., Bierman, P. R., Neilson, T. B., and Rood, D. H., 2018, Agricultural land use doubled sediment loads in western China's rivers: Anthropocene, v. 21, p. 95-106.

Schmidt, A. H., Neilson, T. B., Bierman, P. R., Rood, D. H., Ouimet, W. B., and Sosa Gonzalez, V., 2016, Influence of topography and human activity on apparent in situ 10Be-derived erosion rates in Yunnan, SW China: Earth Surf. Dynam., v. 4, no. 4, p. 819-830.

Seymour, D. B., Green, G. R., and Calver, C. R., 2006, The geology and mineral deposits of Tasmania: A summary: Mineral Resources Tasmania, https://www.mrt.tas.gov.au/products/publications/the_geology_and_mineral_deposits_of_tasmania_a_summary.

Siame, L., Angelier, J., Chen, R.-F., Godard, V., Derrieux, F., Bourlès, D., Braucher, R., Chang, K.-J., Chu, H.-T., and Lee, J.-C., 2011, Erosion rates in an active orogen (NE-Taiwan): A confrontation of cosmogenic measurements with river suspended loads: Quaternary Geochronology, v. 6, no. 2, p. 246-260.

Singleton, A. A., Schmidt, A. H., Bierman, P. R., Rood, D. H., Neilson, T. B., Greene, E. S., Bower, J. A., Perdrial, N., 2016, Effects of grain size, mineralogy, and acid-extractable grain coatings on the distribution of the fallout radionuclides ^{7}Be, ^{10}Be, ^{137}Cs, and ^{210}Pb in river sediment: Geochimica et Cosmochimica Acta, v. 197, p. 71-86.

Starke, J., Ehlers, T., and Schaller, M., 2017, Tectonic and climatic controls on the spatial distribution of denudation rates in Northern Chile (18 S to 23 S) determined from cosmogenic nuclides: Journal of Geophysical Research: Earth Surface, v. 122, no. 10, p. 1949-1971.

-, 2020, Latitudinal effect of vegetation on erosion rates identified along western South America: Science, v. 367, no. 6484, p. 1358-1361.

Stone, J., 1998, A Rapid Fusion Method for Separation of Beryllium-10 From Soils and Silicates: Geochimica et Cosmochimica Acta, v. 62, no. 3, p. 555-561.

-, 2000. Air pressure and cosmogenic isotope production: Journal of Geophysical Research, v. 105, no. B10, p. 23,753–23,759.

Sutherland, R., King, P., and Wood, R., 2001, Tectonic evolution of Cretaceous rift basins in south-eastern Australia and New Zealand: Implications for exploration risk assessment, Petroleum Exploration Society of Australia Eastern Australasian Basins Symposium: Melbourne, Victoria, Australia.

Tomkins, K. M., Humphreys, G. S., Wilkinson, M. T., Fink, D., Hesse, P. P., Doerr, S. H., Shakesby, R. A., Wallbrink, P. J., and Blake, W. H., 2007, Contemporary versus long-term denudation along a passive plate margin: the role of extreme events: Earth Surface Processes and Landforms, v. 32, no. 7, p. 1013-1031.

Valette-Silver, J. N., Brown, L., Pavich, M., Klein, J., and Middleton, R., 1986, Detection of erosion events using10Be profiles: example of the impact of agriculture on soil erosion in the Chesapeake Bay area (U.S.A.): Earth and Planetary Science Letters, v. 80, no. 1, p. 82-90.

van Dongen, R., Scherler, D., Wittmann, H., and von Blanckenburg, F., 2019, Cosmogenic 10Be in river sediment: where grain size matters and why: Earth Surf. Dynam., v. 7, no. 2, p. 393-410.

van Geen, A., Valette-Silver, N. J., Luoma, S. N., Fuller, C. C., Baskaran, M., Tera, F., and Klein, J., 1999, Constraints on the sedimentation history of San Francisco Bay from 14C and 10Be: Marine Chemistry, v. 64, no. 1, p. 29-38.

Vanacker, V., von Blanckenburg, F., Govers, G., Molina, A., Poesen, J., Deckers, J., and Kubik, P., 2007, Restoring dense vegetation can slow mountain erosion to near natural benchmark levels: Geology, v. 35, no. 4, p. 303-306.

von Blanckenburg, F., Bouchez, J., and Wittmann, H., 2012, Earth surface erosion and weathering from the 10Be (meteoric)/9Be ratio: Earth and Planetary Science Letters, v. 351-352, p. 295-305.

Webb, M. A., Kidd, D., and Minasny, B., 2020. Near real-time mapping of air temperature at high spatiotemporal resolutions in Tasmania, Australia: Theoretical and Applied Climatology, v. 141, p. 1181–1201.

Webb, M., Pirie, A., Kidd, D., and Minasny, B., 2018, Spatial analysis of frost risk to determine viticulture suitability in Tasmania, Australia: Australian Journal of Grape and Wine Research, v. 24, no. 2, 219–233.

Weissel, J. K., and Hayes, D. E., 1977, Evolution of the Tasman Sea reappraised: Earth and Planetary Science Letters, v. 36, no. 1, p. 77-84.

West, A. J., Galy, A., and Bickle, M., 2005, Tectonic and climatic controls on silicate weathering: Earth and Planetary Science Letters, v. 235, p. 211–228.

Wilford, J., Searle, R., Thomas, M., Pagendam, D. E., and Grundy, M., 2016. A regolith depth map of the Australian continent: Geoderma, v. 266, p. 1–13.

Willenbring, J. K., and von Blanckenburg, F., 2010, Meteoric cosmogenic Beryllium-10 adsorbed to river sediment and soil: Applications for Earth-surface dynamics: Earth-Science Reviews, v. 98, no. 1, p. 105-122.

Wilson, C. J., 1999, Effects of logging and fire on runoff and erosion on highly erodible granitic soils in Tasmania: Water Resources Research, v. 35, no. 11, p. 3531-3546.

Wittmann, H., Malusà, M. G., Resentini, A., Garzanti, E., and Niedermann, S., 2016, The cosmogenic record of mountain erosion transmitted across a foreland basin: Source-to-sink analysis of in situ 10Be, 26Al and 21Ne in sediment of the Po river catchment: Earth and Planetary Science Letters, v. 452, p. 258-271.

Wittmann, H., Oelze, M., Gaillardet, J., Garzanti, E., and von Blanckenburg, F., 2020, A global rate of denudation from cosmogenic nuclides in the Earth's largest rivers: Earth-Science Reviews, v. 204, p. 103147.

Wittmann, H., von Blanckenburg, F., Bouchez, J., Dannhaus, N., Naumann, R., Christl, M., and Gaillardet, J., 2012, The dependence of meteoric 10Be concentrations on particle size in Amazon River bed sediment and the extraction of reactive 10Be/9Be ratios: Chemical Geology, v. 318-319, p. 126-138.

Wittmann, H., von Blanckenburg, F., Dannhaus, N., Bouchez, J., Gaillardet, J., Guyot, J. L., Maurice, L., Roig, H., Filizola, N., and Christl, M., 2015, A test of the cosmogenic 10Be(meteoric)/9Be proxy for simultaneously determining basin-wide erosion rates, denudation rates, and the degree of weathering in the Amazon basin: Journal of Geophysical Research: Earth Surface, v. 120, no. 12, p. 2498-2528.

Wittmann, H., von Blanckenburg, F., Guyot, J.-L., Maurice, L., and Kubik, P., 2011, Quantifying sediment discharge from the Bolivian Andes into the Beni foreland basin from cosmogenic 10Be-derived denudation rates: Revista Brasileira de Geociências, v. 41, no. 4, p. 629-641.

Wittmann, H., von Blanckenburg, F., Guyot, J. L., Maurice, L., and Kubik, P. W., 2009, From source to sink: Preserving the cosmogenic 10Be-derived denudation rate signal of the Bolivian Andes in sediment of the Beni and Mamoré foreland basins: Earth and Planetary Science Letters, v. 288, no. 3, p. 463-474.

Yanites, B. J., Tucker, G. E., and Anderson, R. S., 2009, Numerical and analytical models of cosmogenic radionuclide dynamics in landslide-dominated drainage basins: Journal of Geophysical Research: Earth Surface, v. 114, no. F1.

You, C.F., Lee, T., and Li, Y.H., 1989. The partition of Be between soil and water: Chemical Geology, v. 77, p. 105–118.